



**HAL**  
open science

# Numerical investigation of a high order hybridizable discontinuous Galerkin method for 2d time-harmonic Maxwell's equations

Liang Li, Stéphane Lanteri, Ronan Perrussel

► **To cite this version:**

Liang Li, Stéphane Lanteri, Ronan Perrussel. Numerical investigation of a high order hybridizable discontinuous Galerkin method for 2d time-harmonic Maxwell's equations. *COMPEL: The International Journal for Computation and Mathematics in Electrical and Electronic Engineering*, 2013, pp. 1112 - 1138. 10.1108/03321641311306196 . hal-00906142

**HAL Id: hal-00906142**

**<https://hal.science/hal-00906142>**

Submitted on 21 Nov 2013

**HAL** is a multi-disciplinary open access archive for the deposit and dissemination of scientific research documents, whether they are published or not. The documents may come from teaching and research institutions in France or abroad, or from public or private research centers.

L'archive ouverte pluridisciplinaire **HAL**, est destinée au dépôt et à la diffusion de documents scientifiques de niveau recherche, publiés ou non, émanant des établissements d'enseignement et de recherche français ou étrangers, des laboratoires publics ou privés.

# Numerical investigation of a high order hybridizable discontinuous Galerkin method for 2d time-harmonic Maxwell's equations

Liang Li\*

Stéphane Lanteri<sup>†</sup>

Ronan Perrussel<sup>‡</sup>

## 1 Introduction

Discontinuous Galerkin (DG) methods have been extensively studied in the recent years (Arnold *et al.*, 2002)-(Cockburn and Shu, 1989)-(Cockburn and Shu, 1998). A DG method can be viewed as a clever combination of a finite element method (FE) and a finite volume method (FV) (Hesthaven and Warburton, 2008). A space of basis and test functions is defined as in the FE method on one hand, while the equation is satisfied in a sense closer to the FV method on the other hand. Ideally, the DG methods share almost all the advantages of the FE and the FV methods: adaptivity to complex geometries, easily obtained high order accuracy, *hp*-adaptivity and natural parallelism.

DG methods have been considered for the convection-diffusion equation (Cockburn and Shu, 1998), model elliptic equations (Arnold *et al.*, 2002) and the Helmholtz equation (Feng and Wu, 2009)-(Feng and Xin, 2012). For Maxwell's equations, DG methods have been developed for both time-transient (Hesthaven and Warburton, 2002)-(Fezoui *et al.*, 2005)-(Cohen *et al.*, 2006) and time-harmonic problems (Houston *et al.*, 2004)-(Houston *et al.*, 2005)-(Dolean *et al.*, 2008). Despite many advantages, the DG methods have one main drawback particularly sensitive for stationary problems: the number of globally coupled Degrees Of Freedom (DOFs) is  $\sum_{i=1}^{N_t} \text{Ndof}_i$  with  $N_t$  being the number of elements and  $\text{Ndof}_i$  being the number of DOFs on element  $i$ , which is greater than the number of DOFs used by conforming FE methods for the same accuracy. For instance, with triangular meshes in 2d the total number of DOFs for the complete first order edge element method (Nedelec, 1986) is  $2N_f$  with  $N_f$  being the number of edges, while the total number of DOFs of the first order DG method is  $9N_t$ . Since  $N_t \approx \frac{2}{3}N_f$  in a triangular mesh, the number of DOFs of the DG method is approximately three times as large as that of the edge element method for a first order approximation for both methods. Consequently, the DG methods are expensive both in terms of CPU time and memory consumption, especially for time-harmonic problems. Hybridization of DG methods (Cockburn *et al.*, 2009) is devoted to address this issue while keeping all the advantages of DG methods.

The hybridizable discontinuous Galerkin (HDG) methods introduce an additional *hybrid* variable on the faces of the elements, with which the local solutions can be determined. A so-called *conservativity condition* is imposed on the numerical flux, whose expression involved the hybrid variable, at the interface between neighboring elements. As a result, the HDG methods produce a linear system in terms of the degrees of freedom of the additional hybrid variable only. In this way, the number of globally coupled DOFs is drastically reduced. The local solutions of the electromagnetic fields can then be obtained by solving local problems element-by-element. Optimal convergence properties of some HDG methods have been obtained or demonstrated numerically for the convection-diffusion equations (Nguyen *et al.*, 2009)-(Nguyen *et al.*, 2009), the Helmholtz equation (Griesmaier and Monk, 2011), and 2d Maxwell's equations (Nguyen *et al.*, 2011). The method that we study in this paper actually coincides with the method referred as HDGII in (Nguyen *et al.*, 2011) (up to a scaling factor). Moreover, since in 2d Maxwell's equations are similar to Helmholtz'

---

\*School of Mathematical Sciences, University of Electronic Science and Technology of China, Chengdu, China.

<sup>†</sup>Nachos Project-Team, INRIA Sophia Antipolis-Méditerranée, Sophia Antipolis, France.

<sup>‡</sup>LAPLACE (LABoratoire PLasma et Conversion d'Énergie), Université de Toulouse, CNRS/INPT/UPS, Toulouse, France.

equation up to the rotation of the transverse field, our HDG method is also closely related to the formulation theoretically studied in (Griesmaier and Monk, 2011).

In contrast with the work of (Nguyen *et al.*, 2011) where a similar formulation has been introduced, our presentation puts more emphasis on the implementation aspects in the spirit of (Kirby *et al.*, 2012), and on the computational performance assessment of the method in comparison with an equivalent upwind flux-based DG formulation. Besides, we propose two methodological extensions in view of the application of the method to more realistic propagation problems. First, we introduce a direct extension of the formulation adopted in (Nguyen *et al.*, 2011) in order to consider both an absorbing boundary condition and a perfectly electric conductor boundary condition (the latter being the only boundary condition considered in (Nguyen *et al.*, 2011)) in the definition of the boundary value problem for the 2d transverse magnetic Maxwell equations. Second, we address the issue of taking into account geometries with curved boundaries. Several authors have studied this aspect, see (Bassi and Rebay, 1997)-(Fahs, 2010)-(Krivodonova and Berger, 2006)-(Zlámal, 1973) and references therein. In (Luo *et al.*, 2001), the authors study the importance of using properly curved mesh entities to get feasible high order discretizations over curved domains. (Bassi and Rebay, 1997) show that, in the presence of curved boundaries, a meaningful high order accurate solution can be obtained only if a corresponding high order approximation of the geometry is employed. (Fahs, 2010) has proposed an isoparametric technique combined with a high order DG formulation to solve the time-transient Maxwell equations. The author finds that, under  $p$ -refinement, exponential convergence is achieved with quadratic and cubic geometric approximations while the linear approximation leads to no improvement of accuracy. Unsurprisingly, when we deal with curved computational domains, a linear approximation of the geometry will confine the convergence order of our HDG method to 2. We thus resort to a higher order geometric approximation to gain optimal convergence of the HDG method. Both quadratic and cubic mappings are studied.

This article is organized as follows. In section 2, we present 2d Maxwell's equations and give some notations that will be used throughout this paper. In section 3, we propose a HDG formulation and discuss the link between classical upwind flux DG formulation and the HDG formulation. Some properties of the local problems and of the global reduced problem are also stated. Section 4 consists of the implementation details of the discretization of our HDG formulation. Section 5 is devoted to the treatment of curved elements, especially the evaluation of integrals over curved elements through both quadratic and cubic mappings. Numerical results are given in section 6. Finally, in section 7 we draw some concluding remarks.

## 2 Problem statement and notations

### 2.1 Time-harmonic Maxwell's equations in 2d

We aim at solving time-harmonic Maxwell's equations in 2d (here a transverse magnetic setting is considered) without volume source term for sake of simplicity<sup>1</sup>

$$i\omega\varepsilon_r E - \mathbf{curl} \mathbf{H} = 0, \text{ in } \Omega \quad \text{and} \quad i\omega\mu_r \mathbf{H} + \mathbf{curl} E = 0, \text{ in } \Omega, \quad (1)$$

where  $i$  is the imaginary unit,  $\omega$  is the angular frequency,  $\varepsilon_r$  and  $\mu_r$  are the relative electric permittivity and magnetic permeability,  $E = E_z$  and  $\mathbf{H} = (H_x \ H_y)$  denote the electric and magnetic fields. The boundary conditions are given by

$$\begin{cases} E = 0, & \text{on } \Gamma_m, \\ E + (\mathbf{n} \times \mathbf{H}) = E^{\text{inc}} + (\mathbf{n} \times \mathbf{H}^{\text{inc}}) = g^{\text{inc}}, & \text{on } \Gamma_a, \end{cases} \quad (2)$$

with  $\Gamma_m \cup \Gamma_a = \partial\Omega$ ,  $\Gamma_m \cap \Gamma_a = \emptyset$ ,  $\mathbf{n}$  the outward unit norm vector on  $\partial\Omega$ , and  $E^{\text{inc}}$ ,  $\mathbf{H}^{\text{inc}}$  an incident electromagnetic wave. The first relation of (2) indicates a metallic boundary condition (also called perfect electric conductor condition) on  $\Gamma_m$ , while the second relation states a Silver-Müller (first order absorbing boundary) condition on  $\Gamma_a$ . The differential operators in this 2d setting are

$$\mathbf{curl} E = (\partial_y E \quad -\partial_x E) \quad \text{and} \quad \mathbf{curl} \mathbf{H} = \partial_x H_y - \partial_y H_x,$$

---

<sup>1</sup>A volume source can be straightforwardly added.

and the cross-product of two vectors is  $\mathbf{u} \times \mathbf{v} = u_x v_y - u_y v_x$ .

## 2.2 Notations

A triangulation  $\mathcal{T}_h$  of  $\Omega$  is considered with  $K$  denoting an element (a triangle) of the mesh. We denote by  $\mathcal{F}_h^I$  the union of all interior interfaces (edges in the present 2d case, anyhow, we call them faces) of  $\mathcal{T}_h$ , by  $\mathcal{F}_h^B$  the union of all the boundary interfaces of  $\mathcal{T}_h$ , and by  $\mathcal{F}_h = \mathcal{F}_h^I \cup \mathcal{F}_h^B$ . For an interface  $F = \overline{K^+} \cap \overline{K^-} \in \mathcal{F}_h^I$ , let  $(\mathbf{v}^\pm, v^\pm)$  be the traces of  $(\mathbf{v}, v)$  on  $F$  from the interior of  $K^\pm$ . On this face, we define *mean (average) values*  $\{\cdot\}$  and *jumps*  $\llbracket \cdot \rrbracket$  as follows

$$\left\{ \begin{array}{l} \{\mathbf{v}\}_F = \frac{1}{2}(\mathbf{v}^+ + \mathbf{v}^-), \\ \{v\}_F = \frac{1}{2}(v^+ + v^-), \\ \llbracket \mathbf{n} \times \mathbf{v} \rrbracket_F = \mathbf{n}^+ \times \mathbf{v}^+ + \mathbf{n}^- \times \mathbf{v}^-, \\ \llbracket v \mathbf{t} \rrbracket_F = v^+ \mathbf{t}^+ + v^- \mathbf{t}^-, \end{array} \right.$$

where  $\mathbf{n}^\pm$  denotes the outward unit norm vector to  $K^\pm$  and  $\mathbf{t}^\pm$  denotes the unit tangent vectors to the boundaries  $\partial K^\pm$  such that  $\mathbf{t}^+ \times \mathbf{n}^+ = 1$  and  $\mathbf{t}^- \times \mathbf{n}^- = 1$ . For the boundary faces these expressions are modified as (assuming  $F = \partial K^+ \cap \partial \Omega$ )

$$\left\{ \begin{array}{l} \{\mathbf{v}\}_F = \mathbf{v}^+, \\ \{v\}_F = v^+, \\ \llbracket \mathbf{n} \times \mathbf{v} \rrbracket_F = \mathbf{n}^+ \times \mathbf{v}^+, \\ \llbracket v \mathbf{t} \rrbracket_F = v^+ \mathbf{t}^+. \end{array} \right.$$

Let  $\mathbb{P}_p(D)$  denote the space of polynomial functions of degree at most  $p$  on a domain  $D$ . For any element  $K \in \mathcal{T}_h$ , let  $V^p(K)$  be the space  $\mathbb{P}_p(K)$  and  $\mathbf{V}^p(K)$  the space  $(\mathbb{P}_p(K))^2$ . The discontinuous finite element spaces are then defined by

$$\begin{aligned} V_h^p &= \{v \in L^2(\Omega) \mid v|_K \in V^p(K), \forall K \in \mathcal{T}_h\}, \\ \mathbf{V}_h^p &= \{\mathbf{v} \in (L^2(\Omega))^2 \mid \mathbf{v}|_K \in \mathbf{V}^p(K), \forall K \in \mathcal{T}_h\}, \end{aligned}$$

where  $L^2(\Omega)$  is the space of square integrable functions on the domain  $\Omega$ . We also introduce a traced finite element space which takes into account the metallic boundary condition

$$M_h^p = \{\eta \in L^2(\mathcal{F}_h) \mid \eta|_F \in \mathbb{P}_p(F), \forall F \in \mathcal{F}_h \text{ and } \eta|_{\Gamma_m} = 0\}.$$

Note that  $M_h^p$  consists of functions which are continuous on an edge, but discontinuous at its ends. For two vectorial functions  $\mathbf{u}$  and  $\mathbf{v}$  in  $(L^2(D))^2$ , we denote  $(\mathbf{u}, \mathbf{v})_D = \int_D \mathbf{u} \cdot \bar{\mathbf{v}} dx$  where  $\bar{\cdot}$  denotes the complex conjugation, while for functions  $u$  and  $v$  in  $L^2(D)$ , we denote  $(u, v)_D = \int_D u \bar{v} dx$  provided  $D$  is a domain in  $\mathbb{R}^2$ , and we denote  $\langle u, v \rangle_F = \int_F u \bar{v} ds$  if  $F$  is a curve. Accordingly, for the whole triangulation we have

$$\begin{aligned} (\cdot, \cdot)_{\mathcal{T}_h} &= \sum_{K \in \mathcal{T}_h} (\cdot, \cdot)_K, & \langle \cdot, \cdot \rangle_{\partial \mathcal{T}_h} &= \sum_{K \in \mathcal{T}_h} \langle \cdot, \cdot \rangle_{\partial K}, \\ \langle \cdot, \cdot \rangle_{\mathcal{F}_h} &= \sum_{F \in \mathcal{F}_h} \langle \cdot, \cdot \rangle_F, & \langle \cdot, \cdot \rangle_{\Gamma_a} &= \sum_{F \in \mathcal{F}_h \cap \Gamma_a} \langle \cdot, \cdot \rangle_F. \end{aligned}$$

### 3 Formulation of the HDG method

#### 3.1 Principles

The DG method seeks an approximate solution  $(E_h, \mathbf{H}_h)$  in the space  $V_h^p \times \mathbf{V}_h^p$  that should satisfy for all  $K$  in  $\mathcal{T}_h$

$$\begin{cases} (i\omega\varepsilon_r E_h, v)_K - (\text{curl } \mathbf{H}_h, v)_K = 0, \quad \forall v \in V^p(K), \\ (i\omega\mu_r \mathbf{H}_h, \mathbf{v})_K + (\mathbf{curl } E_h, \mathbf{v})_K = 0, \quad \forall \mathbf{v} \in \mathbf{V}^p(K). \end{cases}$$

Applying appropriate Green's formulas and replacing the boundary terms by *numerical traces*  $\widehat{E}_h$  and  $\widehat{\mathbf{H}}_h$ , we have

$$\begin{cases} (i\omega\varepsilon_r E_h, v)_K - (\mathbf{H}_h, \mathbf{curl } v)_K - \langle \mathbf{n} \times \widehat{\mathbf{H}}_h, v \rangle_{\partial K} = 0, \quad \forall v \in V^p(K), \\ (i\omega\mu_r \mathbf{H}_h, \mathbf{v})_K + (E_h, \mathbf{curl } \mathbf{v})_K - \langle \widehat{E}_h, \mathbf{n} \times \mathbf{v} \rangle_{\partial K} = 0, \quad \forall \mathbf{v} \in \mathbf{V}^p(K). \end{cases} \quad (3)$$

In the following, we give a formulation to define  $(E_h, \mathbf{H}_h)$  in terms of a hybrid unknown  $\lambda_h$  only. The new variable  $\lambda_h \in M_h^p$  is introduced mainly to replace the numerical trace  $\widehat{E}_h$  which can now be written as

$$\widehat{E}_h = \begin{cases} \lambda_h \text{ for } F \in \mathcal{F}_h^I \cup \{\mathcal{F}_h^B \cap \Gamma_a\} \\ 0 \text{ for } F \in \mathcal{F}_h^B \cap \Gamma_m \end{cases} = \lambda_h, \quad \forall F \in \mathcal{F}_h. \quad (4)$$

Thus  $\widehat{E}_h$  is *single-valued* on each face. We then consider a local numerical trace  $\widehat{\mathbf{H}}_h$  of the form

$$\widehat{\mathbf{H}}_h = \mathbf{H}_h + \tau(E_h - \lambda_h)\mathbf{t} \text{ on } \partial K, \quad (5)$$

where  $\tau > 0$  is a local stabilization parameter (*i.e.* that can be defined for each face based on values assigned at the element level). Adding the contributions of (3) over all elements and enforcing the continuity of the *tangential component* of  $\widehat{\mathbf{H}}_h$ , we can formulate a problem which is to find  $(E_h, \mathbf{H}_h, \lambda_h) \in V_h^p \times \mathbf{V}_h^p \times M_h^p$  such that

$$\begin{cases} (i\omega\varepsilon_r E_h, v)_{\mathcal{T}_h} - (\mathbf{H}_h, \mathbf{curl } v)_{\mathcal{T}_h} - \langle \mathbf{n} \times \widehat{\mathbf{H}}_h, v \rangle_{\partial \mathcal{T}_h} = 0, \quad \forall v \in V_h^p, \\ (i\omega\mu_r \mathbf{H}_h, \mathbf{v})_{\mathcal{T}_h} + (E_h, \mathbf{curl } \mathbf{v})_{\mathcal{T}_h} - \langle \lambda_h, \mathbf{n} \times \mathbf{v} \rangle_{\partial \mathcal{T}_h} = 0, \quad \forall \mathbf{v} \in \mathbf{V}_h^p, \\ \langle \llbracket \mathbf{n} \times \widehat{\mathbf{H}}_h \rrbracket, \eta \rangle_{\mathcal{F}_h} + \langle \lambda_h, \eta \rangle_{\Gamma_a} = \langle g^{\text{inc}}, \eta \rangle_{\Gamma_a}, \quad \forall \eta \in M_h^p, \end{cases} \quad (6)$$

where the last equation is called the *conservativity condition*. Note that we also take the absorbing boundary condition into consideration in the formulation of this conservativity condition. From the expression (5) of  $\widehat{\mathbf{H}}_h$ , once  $\lambda_h$  is known, we can obtain the local solution through (3) due to the discontinuous nature of  $V_h^p$  and  $\mathbf{V}_h^p$ . Moreover, we can eliminate  $E_h$  and  $\mathbf{H}_h$  via the first two equations of (6) to obtain a weak formulation in terms of  $\lambda_h$  only. For an interior face  $F = \partial K^+ \cap \partial K^-$  we have

$$\begin{aligned} \langle \llbracket \mathbf{n} \times \widehat{\mathbf{H}}_h \rrbracket, \eta \rangle_F &= \langle \llbracket \mathbf{n} \times (\mathbf{H}_h + \tau(E_h - \lambda_h)\mathbf{t}) \rrbracket, \eta \rangle_F \\ &= \langle \mathbf{n}^+ \times \mathbf{H}_h^+, \eta \rangle_{\partial K^+} + \langle \mathbf{n}^- \times \mathbf{H}_h^-, \eta \rangle_{\partial K^-} \\ &\quad - \langle \tau^+ E_h^+, \eta \rangle_{\partial K^+} - \langle \tau^- E_h^-, \eta \rangle_{\partial K^-} \\ &\quad + \langle \tau^+ \lambda_h, \eta \rangle_{\partial K^+} + \langle \tau^- \lambda_h, \eta \rangle_{\partial K^-}, \end{aligned}$$

thus

$$\langle \llbracket \mathbf{n} \times \widehat{\mathbf{H}}_h \rrbracket, \eta \rangle_{\mathcal{F}_h} = \langle \mathbf{n} \times \mathbf{H}_h, \eta \rangle_{\partial \mathcal{T}_h} - \langle \tau(E_h - \lambda_h), \eta \rangle_{\partial \mathcal{T}_h}. \quad (7)$$

Inserting (7) into (6) and applying an appropriate Green formula again to the first equation of (6), we obtain another equivalent description of the problem (6) which is to search for the approximation  $(E_h, \mathbf{H}_h, \lambda_h) \in V_h^p \times \mathbf{V}_h^p \times M_h^p$  such that

$$\begin{cases} (i\omega\varepsilon_r E_h, v)_{\mathcal{T}_h} - (\text{curl } \mathbf{H}_h, v)_{\mathcal{T}_h} + \langle \tau(E_h - \lambda_h), v \rangle_{\partial \mathcal{T}_h} = 0, \quad \forall v \in V_h^p, \\ (i\omega\mu_r \mathbf{H}_h, \mathbf{v})_{\mathcal{T}_h} + (E_h, \mathbf{curl } \mathbf{v})_{\mathcal{T}_h} - \langle \lambda_h, \mathbf{n} \times \mathbf{v} \rangle_{\partial \mathcal{T}_h} = 0, \quad \forall \mathbf{v} \in \mathbf{V}_h^p, \\ \langle \mathbf{n} \times \mathbf{H}_h, \eta \rangle_{\partial \mathcal{T}_h} - \langle \tau(E_h - \lambda_h), \eta \rangle_{\partial \mathcal{T}_h} + \langle \lambda_h - g^{\text{inc}}, \eta \rangle_{\Gamma_a} = 0, \quad \forall \eta \in M_h^p. \end{cases} \quad (8)$$

Note that the first two equations define the local problems, which are solved element-by-element. The third equation defines the hybrid variable  $\lambda_h$ .

### 3.2 Relationship between HDG and upwind flux DG

The conservativity condition holds on all the interior faces, which means

$$\langle [\mathbf{n} \times \widehat{\mathbf{H}}_h], \eta \rangle_{\mathcal{F}_h^I} = 0, \quad \forall \eta \in M_h^p.$$

From the formulation, we can infer that  $[\mathbf{n} \times \widehat{\mathbf{H}}_h] = 0$  on every interior face on conforming meshes (Cockburn *et al.*, 2009)-(Nguyen *et al.*, 2009)-(Nguyen *et al.*, 2011). Substituting  $\widehat{\mathbf{H}}_h$  with the expression in (5), we have

$$\begin{aligned} [\mathbf{n} \times (\mathbf{H}_h + \tau(E_h - \lambda_h)\mathbf{t})] &= [\mathbf{n} \times \mathbf{H}_h] - [\tau(E_h - \lambda_h)] \\ &= 0, \quad \forall F \in \mathcal{F}_h^I. \end{aligned}$$

For an interior face  $F = \partial K^+ \cap \partial K^-$  it holds that

$$[\mathbf{n} \times \mathbf{H}_h] - \tau^+ E_h^+ - \tau^- E_h^- + (\tau^+ + \tau^-)\lambda_h = 0 \text{ on } F.$$

Solving for  $\lambda_h$ , we obtain (since  $\tau^+ + \tau^- \neq 0$ )

$$\widehat{E}_h = \lambda_h = \frac{1}{\tau^+ + \tau^-}(\tau^+ E_h^+ + \tau^- E_h^-) - \frac{1}{\tau^+ + \tau^-}[\mathbf{n} \times \mathbf{H}_h] \text{ on } F, \quad (9)$$

by recalling the definition (4) of  $\lambda_h$ . Inserting the expression for  $\lambda_h$  into the following identity

$$\mathbf{n}^\pm \times \widehat{\mathbf{H}}_h^\pm = \mathbf{n}^\pm \times \mathbf{H}_h^\pm + \mathbf{n}^\pm \times (\tau^\pm (E_h^\pm - \lambda_h)\mathbf{t}^\pm),$$

we get  $\mathbf{n}^\pm \times \widehat{\mathbf{H}}_h^\pm = \mathbf{n}^\pm \times \widetilde{\mathbf{H}}_h^2$  with

$$\widetilde{\mathbf{H}}_h = \frac{1}{\tau^+ + \tau^-}(\tau^- \mathbf{H}_h^+ + \tau^+ \mathbf{H}_h^-) + \frac{\tau^+ \tau^-}{\tau^+ + \tau^-} [E_h \mathbf{t}] \text{ on } F. \quad (10)$$

This flux  $\widetilde{\mathbf{H}}_h$  is single-valued on  $F$ . The expressions for the numerical fluxes  $\widehat{E}_h$  (9) and  $\widetilde{\mathbf{H}}_h$  (10) suggest a close relationship between the HDG method and the upwind flux-based DG method. In fact, the proposed HDG method is mathematically equivalent to the upwind flux-based scheme used in (Dolean *et al.*, 2008) when the parameter  $\tau$  is uniformly 1 and absorbing conditions are considered on the whole boundary. The expression (10) of  $\widetilde{\mathbf{H}}_h$  also shows that the HDG method (8) is locally conservative as defined in (Arnold *et al.*, 2002) because  $\widetilde{\mathbf{H}}_h$  is single-valued across inter-element boundaries (Cockburn *et al.*, 2009)-(Nguyen *et al.*, 2011).

### 3.3 Well-posedness of the local problems

The problem on an element  $K$  is the local version of the first two equations of (8)

$$\begin{cases} (i\omega \varepsilon_r E_h, v)_K - (\text{curl } \mathbf{H}_h, v)_K + \langle \tau(E_h - \lambda_h), v \rangle_{\partial K} = 0, \quad \forall v \in V^p(K), \\ (i\omega \mu_r \mathbf{H}_h, \mathbf{v})_K + (E_h, \text{curl } \mathbf{v})_K - \langle \lambda_h, \mathbf{n} \times \mathbf{v} \rangle_{\partial K} = 0, \quad \forall \mathbf{v} \in \mathbf{V}^p(K). \end{cases} \quad (11)$$

To prove the well-posedness of this problem, it is sufficient to prove that the solution  $(E_h, \mathbf{H}_h)$  is unique for a given  $\lambda_h$ . In (11), we consider  $v = E_h$  and  $\mathbf{v} = \mathbf{H}_h$  and we obtain by adding both relations

$$\begin{aligned} (i\omega \varepsilon_r E_h, E_h)_K - (\text{curl } \mathbf{H}_h, E_h)_K + \tau_K \langle (E_h - \lambda_h), E_h \rangle_{\partial K} \\ + (i\omega \mu_r \mathbf{H}_h, \mathbf{H}_h)_K + (E_h, \text{curl } \mathbf{H}_h)_K - \tau_K \langle \lambda_h, E_h \rangle_{\partial K} = 0. \end{aligned}$$

---

<sup>2</sup>The normal components  $\mathbf{n}^\pm \cdot \widehat{\mathbf{H}}_h^\pm$  and  $\mathbf{n}^\pm \cdot \widetilde{\mathbf{H}}_h$  can be different but only the tangential components are relevant in the problem considered here. This point is not obvious in the formulation considered in (Nguyen *et al.*, 2011).

which, with  $\lambda_h = 0$ , yields the following equality

$$(i\omega\varepsilon_r E_h, E_h)_K + (i\omega\mu_r \mathbf{H}_h, \mathbf{H}_h)_K + 2\Im((E_h, \text{curl } \mathbf{H}_h)_K) + \tau_K \langle E_h, E_h \rangle_{\partial K} = 0, \quad (12)$$

where the operator  $\Im$  is used to denote the imaginary part. We assume that both  $\varepsilon_r$ ,  $\mu_r$  and  $\tau_K$  are strictly positive real numbers<sup>3</sup>. Considering the real part of (12), we have  $\tau_K \langle E_h, E_h \rangle_{\partial K} = 0$ , which implies that  $E_h = 0$  on  $\partial K$ . We cannot then conclude on the general well-posedness of the local problems because it is possible to have resonant frequency in the relation (12), since we are solving a Dirichlet-like boundary problem on each element. Note however that this problem never showed up in our numerical experiments.

In the sequel the HDG method employing the spaces  $V_h^p$ ,  $\mathbf{V}_h^p$  and  $M_h^p$  is denoted by HDG- $\mathbb{P}_p$ . In the HDG- $\mathbb{P}_1$  and HDG- $\mathbb{P}_2$  cases, all the degrees of freedom are on  $\partial K$ , and thus  $E_h = 0$  on the entire element  $K$ . Thus we have  $\mathbf{H}_h = 0$  on  $K$ , by comparing the imaginary parts of (12) on both sides. As a result, we can ensure at least the well-posedness of the local problems for the HDG- $\mathbb{P}_1$  and HDG- $\mathbb{P}_2$  case. It is coherent with the results stated in (Feng and Xin, 2012) for the HDG- $\mathbb{P}_1$  method<sup>4</sup>.

In the following sections, we assume that the local problems are always well-posed even if the polynomial degree is greater than 2. Moreover, as the local problem matrices have to be assembled and inverted for the assembly of the global matrix (details are given in Section 4) such a ill-posed local problem could be locally detected during the assembly process and the problematic local element refined in order to obtain well-posed problems on the newly created elements and to pursue the assembly of the global matrix.

### 3.4 Characterization of the reduced problem

For any  $\eta \in M_h^p$ , we denote by  $(E_h^\eta, \mathbf{H}_h^\eta)$  the vector fields whose restriction to an element  $K$  of  $\mathcal{T}_h$  is the solution to the local problem

$$\begin{cases} (i\omega\varepsilon_r E_h^\eta, v)_K - (\text{curl } \mathbf{H}_h^\eta, v)_K - \langle \mathbf{n} \times (\widehat{\mathbf{H}}_h^\eta - \mathbf{H}_h^\eta), v \rangle_{\partial K} = 0, \quad \forall v \in V^p(K), \\ (i\omega\mu_r \mathbf{H}_h^\eta, \mathbf{v})_K + (E_h^\eta, \text{curl } \mathbf{v})_K - \langle \eta, \mathbf{n} \times \mathbf{v} \rangle_{\partial K} = 0, \quad \forall \mathbf{v} \in \mathbf{V}^p(K), \end{cases} \quad (13)$$

where the relation (5) is used in the first equation. We explicitly rewrite the reduced problem as

$$a_h(\lambda_h, \eta) = b_h(\eta), \quad \forall \eta \in M_h^p, \quad (14)$$

with

$$\begin{cases} a_h(\lambda_h, \eta) = \langle \llbracket \mathbf{n} \times \widehat{\mathbf{H}}_h^\lambda \rrbracket, \eta \rangle_{\mathcal{F}_h} + \langle \lambda_h, \eta \rangle_{\Gamma_a}, \\ b_h(\eta) = \langle g^{\text{inc}}, \eta \rangle_{\Gamma_a}, \end{cases}$$

where the subscript  $h$  of  $\lambda$  is taken out for simplicity. In the following, we explore some properties of the sesquilinear form  $a_h$ . Summing (13) over all the elements of  $\mathcal{T}_h$ , we obtain the following relations by recalling the definition of  $\llbracket \cdot \rrbracket$

$$\begin{cases} (i\omega\varepsilon_r E_h^\eta, v)_{\mathcal{T}_h} - (\text{curl } \mathbf{H}_h^\eta, v)_{\mathcal{T}_h} - \langle \llbracket \mathbf{n} \times (\widehat{\mathbf{H}}_h^\eta - \mathbf{H}_h^\eta) \rrbracket, v \rangle_{\mathcal{F}_h} = 0, \quad \forall v \in V_h^p, \\ (-i\omega\mu_r \mathbf{v}, \mathbf{H}_h^\eta)_{\mathcal{T}_h} + (\text{curl } \mathbf{v}, E_h^\eta)_{\mathcal{T}_h} - \langle \llbracket \mathbf{n} \times \mathbf{v} \rrbracket, \eta \rangle_{\mathcal{F}_h} = 0, \quad \forall \mathbf{v} \in \mathbf{V}_h^p. \end{cases} \quad (15)$$

<sup>3</sup>In a lossy medium,  $\varepsilon_r$  or/and  $\mu_r$  could have a negative imaginary part. In this case the well-posedness is easier to prove and not studied here.

<sup>4</sup>As mentioned in subsection 3.2, there is a close relationship between the HDG and upwind flux-based DG methods. Moreover, there is also a similarity between 2d Maxwell's equation and Helmholtz' equation. Using both similarities, it can be shown that the method considered here is similar (for some parameter choices) to the method studied in (Feng and Xin, 2012) and then well-posedness results have to be coherent.

Note that the second relation of (15) is obtained by taking the summation in the complex conjugation of the second relation of (13). The sesquilinear form in (14) can now be obtained

$$\begin{aligned}
a_h(\lambda_h, \eta) &= \langle \llbracket \mathbf{n} \times \widehat{\mathbf{H}}_h^\lambda \rrbracket, \eta \rangle_{\mathcal{F}_h} + \langle \lambda_h, \eta \rangle_{\Gamma_a} \\
&= \langle \llbracket \mathbf{n} \times \mathbf{H}_h^\lambda \rrbracket, \eta \rangle_{\mathcal{F}_h} + \langle \llbracket \mathbf{n} \times (\widehat{\mathbf{H}}_h^\lambda - \mathbf{H}_h^\lambda) \rrbracket, \eta \rangle_{\mathcal{F}_h} + \langle \lambda_h, \eta \rangle_{\Gamma_a} \\
&= (-i\omega\mu_r \mathbf{H}_h^\lambda, \mathbf{H}_h^\eta)_{\mathcal{T}_h} + (\text{curl } \mathbf{H}_h^\lambda, E_h^\eta)_{\mathcal{T}_h} + \langle \llbracket \mathbf{n} \times (\widehat{\mathbf{H}}_h^\lambda - \mathbf{H}_h^\lambda) \rrbracket, \eta \rangle_{\mathcal{F}_h} + \langle \lambda_h, \eta \rangle_{\Gamma_a} \\
&\quad (\text{by the second relation of (15), taking } \mathbf{v} = \mathbf{H}_h^\lambda) \\
&= (-i\omega\mu_r \mathbf{H}_h^\lambda, \mathbf{H}_h^\eta)_{\mathcal{T}_h} + (i\omega\varepsilon_r E_h^\lambda, E_h^\eta)_{\mathcal{T}_h} + \langle \llbracket \mathbf{n} \times (\widehat{\mathbf{H}}_h^\lambda - \mathbf{H}_h^\lambda) \rrbracket, (\eta - E_h^\eta) \rangle_{\mathcal{F}_h} \\
&\quad + \langle \lambda_h, \eta \rangle_{\Gamma_a} \quad (\text{by the first relation of (15)}).
\end{aligned}$$

Considering the definition (5) of  $\widehat{\mathbf{H}}_h^\lambda$ , we have:

$$a_h(\lambda_h, \eta) = (-i\omega\mu_r \mathbf{H}_h^\lambda, \mathbf{H}_h^\eta)_{\mathcal{T}_h} + (i\omega\varepsilon_r E_h^\lambda, E_h^\eta)_{\mathcal{T}_h} + \langle \tau(\lambda_h - E_h^\lambda), (\eta - E_h^\eta) \rangle_{\partial\mathcal{T}_h} + \langle \lambda_h, \eta \rangle_{\Gamma_a}. \quad (16)$$

When  $\varepsilon_r$  and  $\mu_r$  are real-valued, we can infer that the corresponding coefficient matrix  $\mathbf{K}$ , whose assembly is detailed in the next section, is complex symmetric and all the eigenvalues lie in the right half-plane of the complex plane, because of the third and fourth term of (16). Moreover, the first two terms define the imaginary part of  $\mathbf{K}$  if  $\varepsilon_r$  and  $\mu_r$  are real-valued. This matrix is similar to the one resulting from the discretization of the wave equation: it is symmetric but indefinite as soon as  $\omega$  is sufficiently large (this point will be assessed in the numerical experiments). It is probably more classical if we multiply (16) by  $i\omega$  in order to obtain

$$\begin{aligned}
i\omega a_h(\lambda_h, \eta) &= (\mu_r(-i\omega \mathbf{H}_h^\lambda), (-i\omega \mathbf{H}_h^\eta))_{\mathcal{T}_h} - \omega^2(\varepsilon_r E_h^\lambda, E_h^\eta)_{\mathcal{T}_h} \\
&\quad + i\omega \langle \tau(\lambda_h - E_h^\lambda), (\eta - E_h^\eta) \rangle_{\partial\mathcal{T}_h} + i\omega \langle \lambda_h, \eta \rangle_{\Gamma_a}.
\end{aligned}$$

We then find the equivalent of the bilinear form given in (Nguyen *et al.*, 2011, Eq. (45)) where they consider  $\mathbf{W}_j^\lambda = -i\omega \mathbf{H}_h^\lambda$  as an unknown instead of  $\mathbf{H}_h^\lambda$ .

## 4 Implementation

In the section we discuss about the main aspects of the implementation of the previously introduced HDG method and we essentially follow the setting and notations adopted in (Kirby *et al.*, 2012). For sake of simplicity, the proposed implementation insures an admissible finite element mesh with possibly curved boundaries. For an element  $K_e$  of index  $e \in [1, N_t]$  where  $N_t$  is the number of elements of  $\mathcal{T}_h$ , let us write the local solution restricted to  $K_e$  as follows

$$\begin{aligned}
E^e &= \sum_{j=1}^{n_p^e} \underline{E}_j^e \varphi_j^e, \\
\mathbf{H}^e &= (H_x^e \quad H_y^e) \quad \text{with} \quad H_u^e = \sum_{j=1}^{N_p^e} \underline{H}_{u,j}^e \varphi_j^e, \quad u \in \{x, y\},
\end{aligned} \quad (17)$$

where  $N_p^e$  is the dimension of  $\mathbb{P}_p(K_e)$  and  $\varphi_j^e$ 's are the (real-valued) local basis functions. Similarly, for a face  $F_f$  of index  $f \in [1, N_f]$  where  $N_f$  is the number of faces of  $\mathcal{T}_h$  (i.e. the cardinal of  $\mathcal{F}_h$ ),  $\lambda$  is represented by

$$\lambda^f = \sum_{j=1}^{N_p^f} \underline{\lambda}_j^f \psi_j^f,$$

where  $N_p^f$  is the dimension of  $\mathbb{P}_p(F_f)$  and  $\psi_j^f$ 's are the (real-valued) local basis functions. Moreover, we denote by  $\sigma(e, l)$  the index  $f$  of the face  $F_f \in \mathcal{F}_h$  which is the  $l$ -th face of element  $K_e \in \mathcal{T}_h$  (with  $l = 1, \dots, 3$ ).

## 4.1 Discretization of local problems

Discretization of the first equation of (11) on the element  $K_e$  leads to

$$i\omega\varepsilon_r\mathbb{M}^e\mathbf{E}^e + (\mathbb{D}_y^e)^T\mathbf{H}_x^e - (\mathbb{D}_x^e)^T\mathbf{H}_y^e + \sum_{l=1}^3\tau^{(e,l)}\mathbb{E}_l^e\mathbf{E}^e - \sum_{l=1}^3\tau^{(e,l)}\mathbb{F}_l^e\boldsymbol{\lambda}^{\sigma(e,l)} = 0,$$

where  $\cdot^T$  is used to denote the matrix transposition. The entries of the local matrices are defined by

$$\begin{cases} \mathbb{M}^e[i, j] = (\varphi_j^e, \varphi_i^e)_{K_e} = \int_{K_e} \varphi_i^e \varphi_j^e \, d\mathbf{x}, \\ \mathbb{D}_u^e[i, j] = (\varphi_j^e, \partial_u \varphi_i^e)_{K_e} = \int_{K_e} (\partial_u \varphi_i^e) \varphi_j^e \, d\mathbf{x}, \text{ with } u \in \{x, y\}, \\ \mathbb{E}_l^e[i, j] = \langle \varphi_j^e, \varphi_i^e \rangle_{\partial K_e^l} = \int_{\partial K_e^l} \varphi_i^e \varphi_j^e \, ds, \\ \mathbb{F}_l^e[i, j] = \langle \psi_j^{\sigma(e,l)}, \varphi_i^e \rangle_{\partial K_e^l} = \int_{\partial K_e^l} \varphi_i^e \psi_j^{\sigma(e,l)} \, ds, \end{cases} \quad (18)$$

where  $\partial K_e^l$  stands for the  $l$ -th face of element  $K_e$ . Similarly, the discretization of the second equation of (11) is

$$\begin{cases} i\omega\mu_r\mathbb{M}^e\mathbf{H}_x^e - \mathbb{D}_y^e\mathbf{E}^e + \sum_{l=1}^3\mathbb{Q}_{yl}^e\boldsymbol{\lambda}^{\sigma(e,l)} = 0, \\ i\omega\mu_r\mathbb{M}^e\mathbf{H}_y^e + \mathbb{D}_x^e\mathbf{E}^e - \sum_{l=1}^3\mathbb{Q}_{xl}^e\boldsymbol{\lambda}^{\sigma(e,l)} = 0, \end{cases}$$

where the matrices  $\mathbb{M}^e$  and  $\mathbb{D}_u^e$  are defined in (18), and

$$\mathbb{Q}_{ul}^e[i, j] = \langle \varphi_i^e, n_u \psi_j^{\sigma(e,l)} \rangle_{\partial K_e^l} = \int_{\partial K_e^l} n_u \varphi_i^e \psi_j^{\sigma(e,l)} \, ds, \quad u \in \{x, y\}, \quad (19)$$

with  $\mathbf{n}^e = (n_x^e \ n_y^e)$  the outward unit norm vector to  $K_e$ . The local linear system on the element  $K_e$  can then be written as

$$\mathbb{A}^e \begin{bmatrix} \mathbf{H}_x^e \\ \mathbf{H}_y^e \\ \mathbf{E}^e \end{bmatrix} + \mathbb{C}^e \begin{bmatrix} \boldsymbol{\lambda}^{\sigma(e,1)} \\ \boldsymbol{\lambda}^{\sigma(e,2)} \\ \boldsymbol{\lambda}^{\sigma(e,3)} \end{bmatrix} = 0, \quad (20)$$

with

$$\mathbb{A}^e = \begin{bmatrix} i\omega\mu_r\mathbb{M}^e & 0 & -\mathbb{D}_y^e \\ 0 & i\omega\mu_r\mathbb{M}^e & \mathbb{D}_x^e \\ (\mathbb{D}_y^e)^T & -(\mathbb{D}_x^e)^T & i\omega\varepsilon_r\mathbb{M}^e + \sum_{l=1}^3\tau^{(e,l)}\mathbb{E}_l^e \end{bmatrix},$$

and

$$\mathbb{C}^e = \begin{bmatrix} \mathbb{Q}_{y1}^e & \mathbb{Q}_{y2}^e & \mathbb{Q}_{y3}^e \\ -\mathbb{Q}_{x1}^e & -\mathbb{Q}_{x2}^e & -\mathbb{Q}_{x3}^e \\ -\tau^{(e,1)}\mathbb{F}_1^e & -\tau^{(e,2)}\mathbb{F}_2^e & -\tau^{(e,3)}\mathbb{F}_3^e \end{bmatrix}.$$

## 4.2 Global discretization for $\lambda$

Suppose that the interior face  $F_f$  of index  $f$  is shared by elements  $K_e$  and  $K_g$  with local index  $l$  and  $k$ , i.e.  $f = \sigma(e, l) = \sigma(g, k)$ . The conservativity condition on  $F_f$  writes as

$$\begin{aligned} & \langle \mathbf{n}^e \times \mathbf{H}_h^e, \eta \rangle_{\partial K_e^l} + \langle \mathbf{n}^g \times \mathbf{H}_h^g, \eta \rangle_{\partial K_g^k} \\ & - \tau^{(e,l)} \langle E_h^e, \eta \rangle_{\partial K_e^l} - \tau^{(g,k)} \langle E_h^g, \eta \rangle_{\partial K_g^k} \\ & + \tau^{(e,l)} \langle \lambda, \eta \rangle_{\partial K_e^l} + \tau^{(g,k)} \langle \lambda, \eta \rangle_{\partial K_g^k} = 0, \quad \forall \eta \in V^p(F_f). \end{aligned}$$

The corresponding discretization is

$$\begin{aligned} & (\mathbb{Q}_{xl}^e)^T \underline{H}_y^e - (\mathbb{Q}_{yl}^e)^T \underline{H}_x^e - \tau^{(e,l)} (\mathbb{F}_l^e)^T \underline{E}^e + \tau^{(e,l)} \mathbb{G}^f \underline{\lambda}^f \\ + & (\mathbb{Q}_{xk}^g)^T \underline{H}_y^g - (\mathbb{Q}_{yk}^g)^T \underline{H}_x^g - \tau^{(g,k)} (\mathbb{F}_k^g)^T \underline{E}^g + \tau^{(g,k)} \mathbb{G}^f \underline{\lambda}^f = 0, \end{aligned} \quad (21)$$

where

$$\mathbb{G}^f[i, j] = \langle \psi_j^f, \psi_i^f \rangle_{F_f} = \int_{F_f} \psi_i^f \psi_j^f \, ds.$$

For a boundary face on  $\Gamma_a$ , (21) is replaced by

$$(\mathbb{Q}_{xl}^e)^T \underline{H}_y^e - (\mathbb{Q}_{yl}^e)^T \underline{H}_x^e - \tau^{(e,l)} (\mathbb{F}_l^e)^T \underline{E}^e + (1 + \tau^{(e,l)}) \mathbb{G}^f \underline{\lambda}^f = \underline{g}^{\text{inc}, f}, \quad (22)$$

where

$$\underline{g}_i^{\text{inc}, f} = \langle g^{\text{inc}}, \psi_i^f \rangle_{F_f} = \int_{F_f} g^{\text{inc}} \psi_i^f \, ds, \quad i = 1, \dots, n_p^f.$$

To get an explicit global system for  $\lambda$ , let us replicate some notations from (Kirby *et al.*, 2012). Let  $N_\lambda^{(e,l)}$  denote the number of degrees of freedom of  $\lambda$  on the face with local index  $l$  of element  $K_e$ , and let  $N_\lambda$  denote the total number of degrees of freedom of  $\lambda$ . We introduce the trace space spreading operator  $\mathcal{A}_{HDG}^e$  as a matrix of size  $N_\lambda^{(e,l)} \times N_\lambda$  which *scatters* the global trace space values to the local vector on  $K^e$  (Kirby *et al.*, 2012). With these notations, we can rewrite the equation for the local solver (20) as

$$\mathbb{A}^e \underline{W}^e + \mathbb{C} \mathcal{A}_{HDG}^e \underline{\Lambda} = 0 \quad \text{with} \quad \underline{W}^e = \begin{pmatrix} \underline{H}_x^e \\ \underline{H}_y^e \\ \underline{E}^e \end{pmatrix}, \quad (23)$$

where  $\underline{\Lambda}$  is the vector gathering all the global trace space information. Adding all the equations involving every interior face (21) and every boundary face (22) element by element we have

$$\sum_{e=1}^{N_t} (\mathcal{A}_{HDG}^e)^T [\mathbb{B}^e \underline{W}^e + \mathbb{L}^e \mathcal{A}_{HDG}^e \underline{\Lambda}] = \sum_{e=1}^{N_t} (\mathcal{A}_{HDG}^e)^T \underline{g}^e = \underline{g},$$

where the sum over elements along with the left application of the transpose of  $\mathcal{A}_{HDG}^e$  allows to gather the element-wise contributions corresponding to faces and

$$\underline{g}^e = \begin{pmatrix} \underline{g}^{\text{inc}, \sigma(e,1)} \\ \underline{g}^{\text{inc}, \sigma(e,2)} \\ \underline{g}^{\text{inc}, \sigma(e,3)} \end{pmatrix},$$

$\underline{g}^{\text{inc}, \sigma(e,l)}$  ( $l = 1, 2, 3$ ) is nontrivial only on the faces lying on the boundary  $\Gamma_a$ . From (21),  $\mathbb{B}^e$  and  $\mathbb{L}^e$  are defined by

$$\mathbb{B}^e = \begin{bmatrix} -(\mathbb{Q}_{y1}^e)^T & (\mathbb{Q}_{x1}^e)^T & -\tau^{(e,1)} (\mathbb{F}_1^e)^T \\ -(\mathbb{Q}_{y2}^e)^T & (\mathbb{Q}_{x2}^e)^T & -\tau^{(e,2)} (\mathbb{F}_2^e)^T \\ -(\mathbb{Q}_{y3}^e)^T & (\mathbb{Q}_{x3}^e)^T & -\tau^{(e,3)} (\mathbb{F}_3^e)^T \end{bmatrix},$$

and

$$\mathbb{L}^e = \begin{bmatrix} \tau^{(e,1)} \mathbb{G}^{\sigma(e,1)} & 0 & 0 \\ 0 & \tau^{(e,2)} \mathbb{G}^{\sigma(e,2)} & 0 \\ 0 & 0 & \tau^{(e,3)} \mathbb{G}^{\sigma(e,3)} \end{bmatrix}.$$

Note that for a boundary face  $f = \sigma(e, l)$ , from (22), the corresponding diagonal block of  $\mathbb{L}^e$  turns out to be  $(1 + \tau^{(e,l)}) \mathbb{G}^{\sigma(e,l)}$ ,  $l$  may be 1, 2 or 3.

Thus, replacing  $\underline{W}^e$  with its solution from the local system (23), we get

$$\sum_{e=1}^{N_t} (\mathcal{A}_{HDG}^e)^T [-\mathbb{B}^e(\mathbb{A}^e)^{-1} \mathbb{C}^e \mathcal{A}_{HDG}^e \underline{\Lambda} + \mathbb{L}^e \mathcal{A}_{HDG}^e \underline{\Lambda}] = \underline{g},$$

with which we obtain a global equation for  $\underline{\Lambda}$ :

$$\mathbf{K} \underline{\Lambda} = \underline{g}, \quad (24)$$

Where

$$\mathbf{K} = \sum_{e=1}^{N_t} (\mathcal{A}_{HDG}^e)^T \mathbb{K}^e \mathcal{A}_{HDG}^e = \sum_{e=1}^{N_t} (\mathcal{A}_{HDG}^e)^T [\mathbb{L}^e - \mathbb{B}^e(\mathbb{A}^e)^{-1} \mathbb{C}^e] \mathcal{A}_{HDG}^e.$$

Thus, the assembly of (24) can be performed as a classical finite element assembly process with a sequence of computations of elementary matrices  $\mathbb{K}^e$ .

## 5 Curvilinear elements

The most important thing related to curvilinear elements is the way to calculate the integrals in (18) and (19). In order to save computing time, the integration on the underlying element is transferred to the integration over the reference element through integration by substitution, *i.e.*

$$\mathcal{I}^{K_e} = \int_{K_e} f(\mathbf{x}) d\mathbf{x} = \int_{\mathcal{K}_r} f(\Psi(\boldsymbol{\xi})) d\Psi(\boldsymbol{\xi}) = \int_{\mathcal{K}_r} f(\Psi(\boldsymbol{\xi})) \|\mathbf{J}_\Psi\| d\boldsymbol{\xi}, \quad (25)$$

where  $\Psi$  is the mapping from the reference element  $\mathcal{K}_r$  to the current element  $K_e$  which will be defined later,  $\|\mathbf{J}_\Psi\|$  denotes the determinant of the Jacobian matrix of the mapping  $\Psi$ . For a standard element with straight edges only, an affine mapping is accurate enough. Then the determinant of the Jacobian matrix  $\|\mathbf{J}_\Psi\|$  is a constant for each element and can be taken out of the integration symbol. However for a curved element, the affine mapping is not accurate enough and higher order mappings are needed. We consider the second order (quadratic) and the third order (cubic) mappings in this paper. In this case  $\|\mathbf{J}_\Psi\|$  is no longer constant and cannot be taken out of the integration. The numerical treatment of curved boundaries in the context of classical (continuous) finite element methods is described in numerous textbooks such as (Solin *et al.*, 2004). The design of a DG method on curvilinear domains for the solution of the time-transient Maxwell equations is described in (Fahs, 2010). Here, we outline the main ingredients of the adaptation of the proposed HDG method to curvilinear domains and we refer to (Lanteri *et al.*, 2011) for more details. Indeed, in the spirit of what is done for a DG method (Fahs, 2010), the numerical treatment of curved boundaries relies on two main ingredients:

- A mapping. We consider a regular triangulation  $\mathcal{T}_h$  of the computational domain  $\bar{\Omega} = \cup_{K_e \in \mathcal{T}_h} \bar{K}_e$  such that each interior element has only straight edges, and each curved element has at most one edge on the curved boundary. Each interior element is considered as a standard element, which is defined by an affine map from the reference element  $\mathcal{K}_r$ . The curved elements are defined as the images of  $\mathcal{K}_r$  through isoparametric mappings. Suppose that  $\mathcal{K}_r = \{(\xi, \zeta) \in \mathbb{R}^2 : \xi, \zeta \geq 0, \xi + \zeta \leq 1\}$  is the reference triangle with vertices  $A_1, A_2$  and  $A_3$  in  $(\xi, \zeta)$  coordinates. The curved element  $K_e$  spanned by three counter-clockwise counted vertices  $(n_1, n_2, n_3)$  is defined by the mapping

$$K_e \ni (x, y) = \Psi(\xi, \zeta) : \mathcal{K}_r \rightarrow \mathbb{R}^2.$$

The three vertices ( $n_1, n_2$  and  $n_3$ ) are enough to define an affine mapping. We need more information to define the quadratic or cubic mapping (see (Lanteri *et al.*, 2011) for more details).

- Integration rules. Integration by substitution leads to the appearance of  $\|\mathbf{J}_\Psi(\boldsymbol{\xi})\|$ , which is a polynomial of total degree 1 for a quadratic mapping, and of total degree 4 for a cubic mapping

$$\|\mathbf{J}_\Psi(\boldsymbol{\xi})\| = \sum_{i,j} J_{ij}^{(m)}(\tilde{n}) \xi^i \zeta^j. \quad (26)$$

The coefficients  $J_{ij}^{(m)}(\tilde{n})$  in (26) are listed below:

- Quadratic case:

$$J_{00}^{(2)} = \mathcal{D}(e_{2,1}, e_{3,1}), \quad J_{10}^{(2)} = 4\mathcal{D}(e_{2,1}, e_{5,5^*}), \quad J_{01}^{(2)} = 4\mathcal{D}(e_{5,5^*}, e_{3,1}).$$

- Cubic case:

$$\begin{aligned} J_{00}^{(3)} &= \mathcal{D}(e_{2,1}, e_{3,1}), & J_{10}^{(3)} &= -\frac{9}{2}(L_1 + L_2), & J_{01}^{(3)} &= \frac{9}{2}(L_3 + L_4), \\ J_{11}^{(3)} &= 27(L_2 - L_3), & J_{20}^{(3)} &= \frac{27}{2}L_1, & J_{02}^{(3)} &= -\frac{27}{2}L_4, \\ J_{21}^{(3)} &= \frac{243}{4}\mathcal{D}(e_{7,7^*}, e_{6,6^*}), & J_{12}^{(3)} &= J_{21}^{(3)}, & J_{22}^{(3)} &= -9J_{21}^{(3)}, \end{aligned}$$

where

$$L_1 = \mathcal{D}(e_{2,1}, e_{6,6^*}), \quad L_2 = \mathcal{D}(e_{2,1}, e_{7,7^*}), \quad L_3 = \mathcal{D}(e_{3,1}, e_{6,6^*}), \quad L_4 = \mathcal{D}(e_{3,1}, e_{7,7^*}).$$

Note that we use  $\mathcal{D}(\mathbf{w}_1, \mathbf{w}_2)$  to denote the determinant of  $(\mathbf{w}_1, \mathbf{w}_2)$  with  $\mathbf{w}_1, \mathbf{w}_2 \in \mathbb{R}^2$ . The symmetric Dunavant cubature formulas (Cools, 2003) are used to calculate the integrations (25). The integrations over the curved edges are also computed through integration by substitution

$$\mathcal{I}^{F_f} = \int_{F_f} f(\mathbf{x}) d\mathbf{x} = \int_{F_f} f(\Phi(t)) d\Phi(t) = \int_{I_r} f(\Phi(t)) \|J_\Phi(t)\| dt,$$

where  $\|J_\Phi(t)\|$  denotes the norm of the differential of the quadratic or cubic mapping  $\Phi$  evaluated in  $t$ . A Gauss-Legendre quadrature is used to compute these line integrals.

## 6 Numerical experiments

In this section, we give some numerical results to show the effectiveness of the considered HDG method. The HDG and DG methods have been implemented in a Fortran 90 code. Simulations are conducted on a workstation equipped with an Intel Xeon 2.67GHz CPU. Our implementation of high order discontinuous Galerkin (DG and HDG) methods makes use of nodal basis functions with equispaced nodes up to order 4. MUMPS (a MUltifrontal Massively Parallel sparse direct Solver) (Amestoy *et al.*, 2000) is used to solve the reduced linear system (24). Two test problems are considered in order to evaluate the method.

### 6.1 Plane wave propagation in vacuum

We first consider a simple problem consisting of the propagation of a plane wave in vacuum. The computational domain is chosen to be the unit square  $\Omega = ]0; 1[^2$  and the Silver Müller absorbing boundary condition is imposed on the whole boundary. The electromagnetic parameters  $\varepsilon_r$  and  $\mu_r$  are set to be 1 everywhere, and unless otherwise stated the angular frequency is  $\omega = 4\pi$  and  $\tau = 1$  in the HDG formulation.

### 6.1.1 Uniform meshes

Uniform triangular meshes are considered in this subsection. We tested both the upwind flux DG method (UF- $\mathbb{P}_p$  denotes the upwind flux DG method of order  $p$ ) and the HDG method (HDG- $\mathbb{P}_p$  denotes the HDG method of order  $p$ ). The numerical convergence results are presented in Figure 1. Compared to the upwind flux DG method, the HDG method can achieve the same accuracy but with less globally coupled degrees of freedom. For 2d Maxwell's equations, the number of unknowns of the HDG method is  $N_{\text{HDG}} = N_f \cdot ndf$ , provided  $N_f$  the number of faces (edges in the 2d case), and  $ndf$  the number of DOFs on each face, while, the number of unknowns of the upwind flux scheme is  $N_{\text{UF}} = 3N_e \cdot nde$ , with  $N_e$  the number of elements (triangles in this case),  $nde$  the number of DOFs on each element. In order to compare,  $N_f \approx 3/2 N_e$ ,  $ndf = p + 1$ , and  $nde = (p + 1)(p + 2)/2$ , so with the increase of the degree of the interpolation polynomials, the reduction of the number of DOFs by the HDG method can be seen more and more evidently. We can also observe in Figure 1 the interest of higher order polynomial approximations which allows a considerable reduction of the number of DOFs. The numerically estimated convergence order (using a linear regression method) of the HDG method is given in Table 1. A detailed comparison between the performances of the

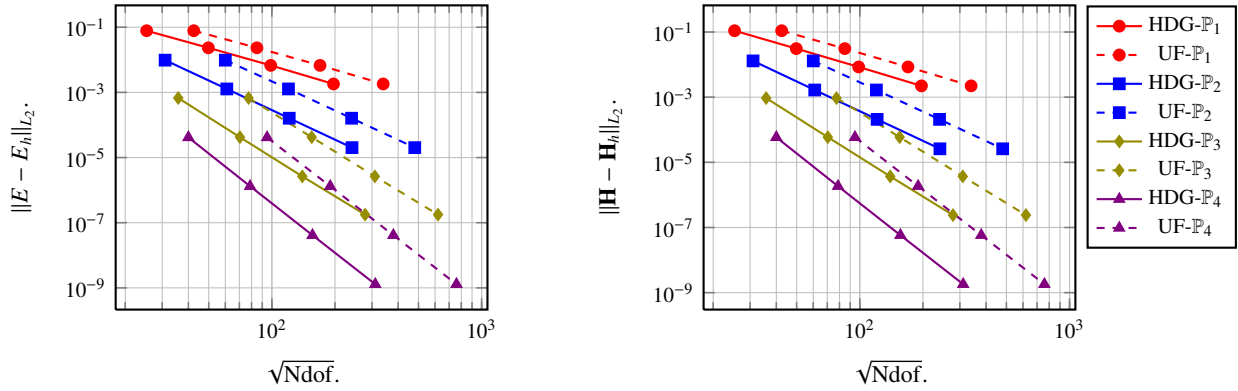


Figure 1:  $L_2$ -error for both  $E$  and  $\mathbf{H}$  fields for several polynomial approximations.  $\text{Ndof}$  is the number of degrees of freedom. HDG- $\mathbb{P}_p$  and UF- $\mathbb{P}_p$ ,  $i = 1, 2, 3, 4$  demonstrate the convergence results for HDG method and upwind flux scheme respectively.

Table 1: Numerical convergence order using the HDG method on uniform meshes.

	$\mathbb{P}_1$	$\mathbb{P}_2$	$\mathbb{P}_3$	$\mathbb{P}_4$
$E$ field	1.8	3.0	4.0	5.0
$\mathbf{H}$ field	1.9	3.0	4.0	5.0

HDG method and the upwind flux DG method is given in Table 2. In Table 2, “MS” denotes the mesh size, “Memory” denotes the memory measured in MB consumed when solving the global linear system by the direct solver MUMPS, “ $T_{\text{construction}}$ ” denotes the CPU time measured in seconds for the construction of the global linear system and “ $T_{\text{solution}}$ ” denotes the CPU time measured in seconds for solving the resulting linear system. It is seen in Table 2 that the HDG method saves the memory cost as well as the required CPU time to yield a given accuracy level. The CPU time for the construction of the global matrix of the HDG method is higher than that of the upwind flux DG method, because in the HDG method we are required to compute  $\mathbb{K}^e = \mathbb{B}^e(\mathbb{A}^e)^{-1}\mathbb{C}^e$  on each element. Note that it is not necessary to explicitly compute the entries of  $(\mathbb{A}^e)^{-1}$ , and that the computation of  $\mathbb{K}^e$  for each element can be done in parallel, which means the construction time can be reduced in a parallel version of the code. However the CPU time for solving the global linear system and the total CPU time consumed by the HDG method are much less than those of the upwind flux DG

Table 2: Comparisons between HDG and upwind flux (UF) DG methods on memory and CPU time.

MS	Memory (MB)		$T_{\text{construction}}$ (s)		$T_{\text{solution}}$ (s)	
	HDG	UF	HDG	UF	HDG	UF
$\mathbb{P}_1$						
0.140	2	5	0.00	0.00	0.01	0.03
0.071	5	19	0.01	0.00	0.02	0.10
0.035	20	85	0.03	0.01	0.04	0.64
0.018	86	389	0.09	0.03	0.52	3.87
$\mathbb{P}_2$						
0.140	3	11	0.01	0.00	0.01	0.07
0.071	9	48	0.03	0.01	0.04	0.35
0.035	41	221	0.09	0.02	0.22	2.06
0.018	187	1024	0.37	0.08	1.27	13.33
$\mathbb{P}_3$						
0.14	4	21	0.02	0.01	0.01	0.14
0.071	15	96	0.08	0.02	0.08	0.77
0.035	71	435	0.29	0.05	0.29	4.63
0.018	327	1955	1.16	0.19	2.54	31.14
$\mathbb{P}_4$						
0.140	5	36	0.05	0.01	0.02	0.30
0.071	24	160	0.21	0.03	0.12	1.45
0.035	106	720	0.80	0.11	0.67	8.29
0.018	499	3258	3.17	0.40	4.54	51.41

method due especially to the reduction of the number of global coupled unknowns<sup>5</sup>

In order to study how the parameter  $\tau$  affects the convergence of the HDG method, we give the errors of both the  $E$  field and  $\mathbf{H}$  field versus different values of  $\tau$  in Figure 2. The results are obtained using the HDG- $\mathbb{P}_3$  scheme on the mesh with mesh size 0.071. Figure 2 shows that the convergence of the HDG method seems to weakly depend on the choice of  $\tau$ . It is easily observed that with the increase of  $\tau$  we have a little more accurate solution for  $E$ , but we lose the accuracy of the solution for  $\mathbf{H}$ . The value of the parameter  $\tau$  can be chosen around 1. In all the following numerical experiments, we set  $\tau = 1$ . The condition numbers of the coefficient matrices of the resulting global linear systems are presented in Table 3. The results for HDG- $\mathbb{P}_1$  and HDG- $\mathbb{P}_3$  are given here, but similar observations can be done for the HDG- $\mathbb{P}_2$  and HDG- $\mathbb{P}_4$  methods. We find that the condition numbers on the same mesh decrease as the frequency of the incident wave grows. The condition number is more dependent on the mesh size and the size of the matrix. This provides a good chance to develop efficient iterative solvers for the resulting linear systems. A similar conclusion has also been made by Griesmaier and Monk in (Griesmaier and Monk, 2011), where they employ an HDG method to solve Helmholtz equation. The distributions of the eigenvalues of the global matrix  $\mathbf{K}$  of (24) for the coarsest mesh, *i.e.*  $h = 0.14$ , are shown in Figure 3. All the eigenvalues have nonnegative (positive in this case) real parts, which is in agreement with the conclusion made in subsection 3.4. From Figure 3, we can also observe that on the same mesh the eigenvalues become clustered as the frequency increases, which agrees with the observations from Table 3. Finally, it can be noticed that the number of eigenvalues with a positive imaginary part increases when  $\omega$  increases for a fixed discretization; this is due to the indefinite and wave equation-like nature of the imaginary part of the matrix as underlined in subsection 3.4.

<sup>5</sup>Probably other properties of the resulting linear systems have an impact on the computing costs but this is not discussed here and is actually the subject of an ongoing research.

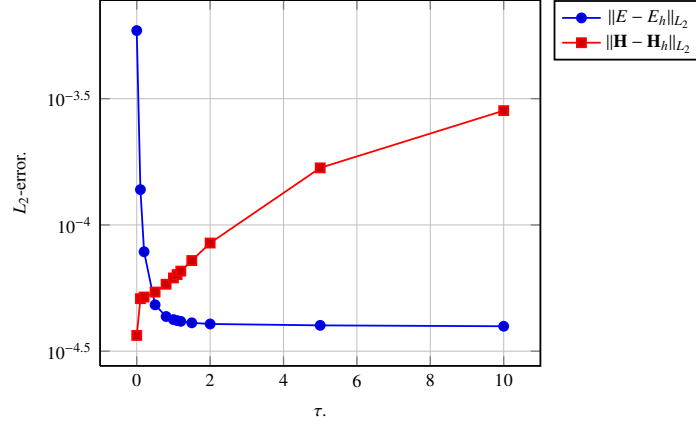


Figure 2: Errors of both  $E$  and  $\mathbf{H}$  field versus  $\tau$  for the HDG- $\mathbb{P}_3$  method.

Table 3: Condition numbers of the coefficient matrices  $\mathbf{K}$  (24) of the reduced system with respect to  $\omega$ .

HDG- $\mathbb{P}_1$				
Mesh size $h$	0.14	0.071	0.035	0.018
$\omega = 2\pi$	1.05e+03	4.07e+03	1.59e+04	6.21e+04
$\omega = 4\pi$	8.13e+02	2.96e+03	1.06e+04	4.19e+04
$\omega = 8\pi$	4.38e+02	2.07e+03	8.36e+03	2.89e+04
$\omega = 16\pi$	8.77e+01	7.39e+02	5.42e+03	2.18e+04
HDG- $\mathbb{P}_3$				
Mesh size $h$	0.14	0.071	0.035	0.018
$\omega = 2\pi$	3.18e+03	1.23e+04	4.91e+04	1.95e+05
$\omega = 4\pi$	2.12e+03	8.27e+03	3.26e+04	1.35e+05
$\omega = 8\pi$	1.57e+03	6.16e+03	2.50e+04	1.01e+05
$\omega = 16\pi$	1.25e+03	4.00e+03	1.77e+04	6.73e+04

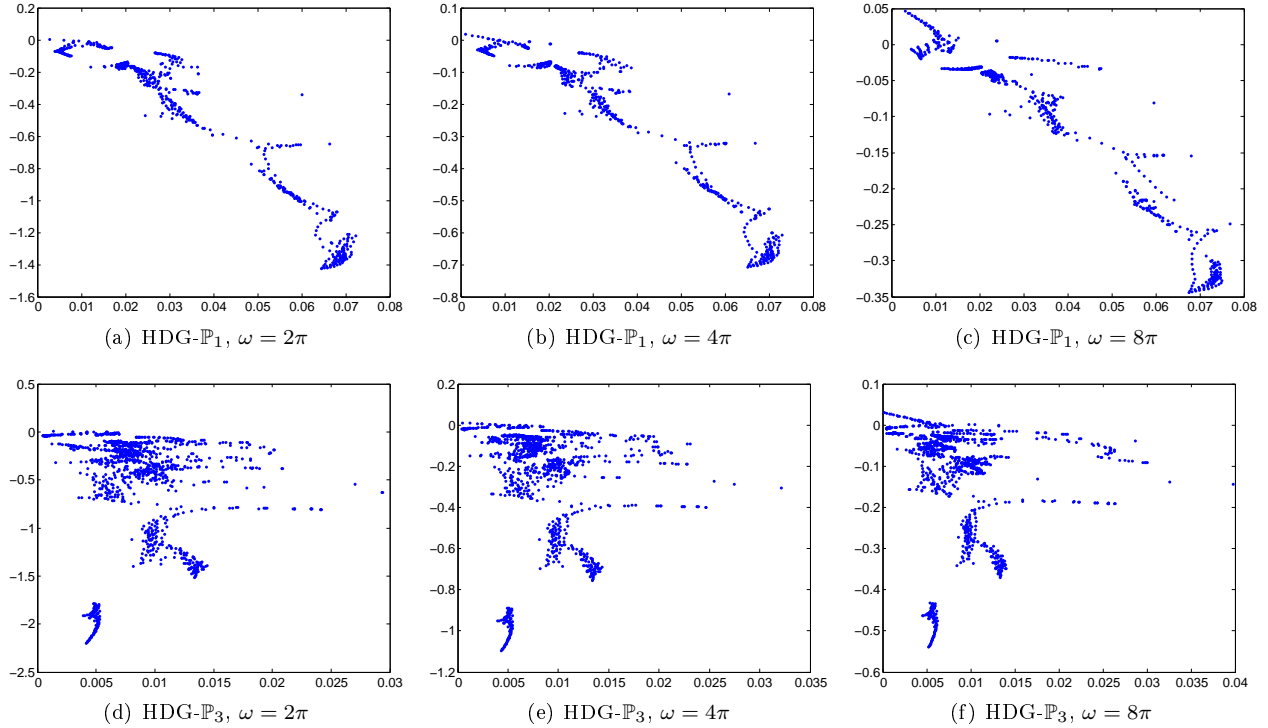


Figure 3: Distributions of the eigenvalues of the global matrix for several angular frequencies.

### 6.1.2 Independently refined non-uniform meshes

Independently refined non-uniform meshes are used in this subsection. Four meshes are involved, and the mesh sizes are 0.184, 0.123, 0.0578 and 0.0289, respectively. Here “Mesh size” refers to the largest edge length of the mesh  $\mathcal{T}_h$ . The first three meshes are given in Figure 4. Numerical convergence results are shown in Figure 5. The estimated numerical convergence orders are given in Table 4. Optimal convergence orders

Table 4: Numerical convergence order using the HDG method on independently refined meshes.

	$\mathbb{P}_1$	$\mathbb{P}_2$	$\mathbb{P}_3$	$\mathbb{P}_4$
$E$ field	2.0	3.1	4.2	5.2
$\mathbf{H}$ field	2.0	3.1	4.2	5.2

are again obtained for both fields  $E$  and  $\mathbf{H}$  on non-uniform meshes, concluded from Figure 1, Figure 5, Table 1 and Table 4. These convergence rates are also theoretically proved in (Griesmaier and Monk, 2011).

## 6.2 Scattering of a plane wave by a metallic cylinder

The electromagnetic scattering of a plane wave by an infinite metallic cylinder is now considered. The radius of the cylinder is taken to be  $\lambda_0$ , where  $\lambda_0$  denotes the wavelength of the incident wave in the vacuum. The artificial absorbing boundary is set to be a concentric circle with radius being  $3\lambda_0$ . The angular frequency is  $\omega = 2\pi$ . We use four independently refined meshes whose characteristics are summarized in Table 5, where  $N_t$  denotes the number of elements,  $N_{sf}$  denotes the number of straight faces and  $N_{cf}$  denotes the number of curved faces. The first three meshes are shown in Figure 6. The convergence history of the HDG method based on the affine mapping is shown in Figure 7. We can see that the asymptotic convergence order for

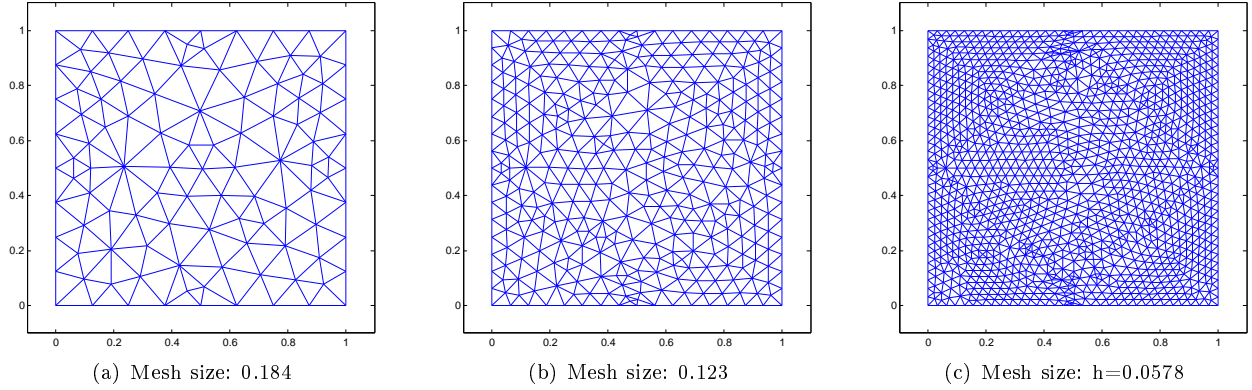


Figure 4: The first three independently refined meshes.

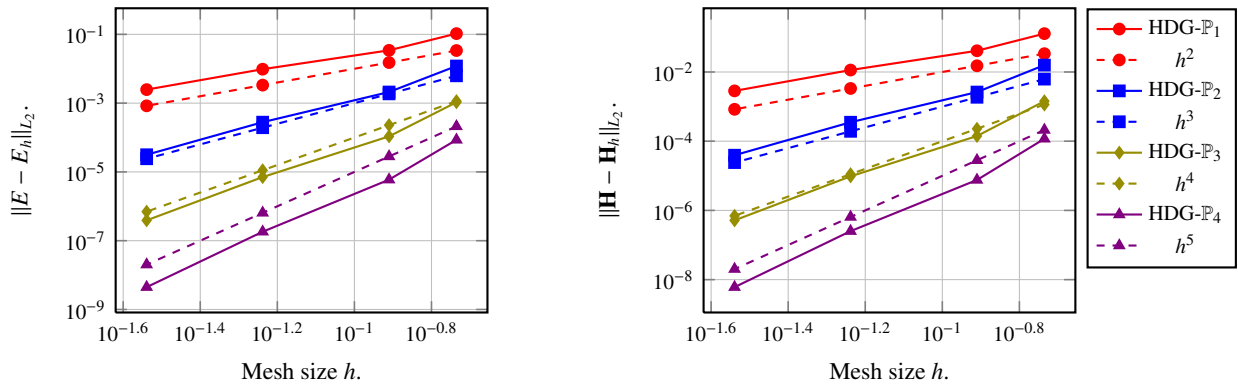


Figure 5: Convergence results of both  $E$  and  $\mathbf{H}$  fields on independently refined meshes.

both  $E$  and  $\mathbf{H}$  is limited to 2. The convergence histories of the HDG method with a quadratic and a cubic mappings are given in Figure 8. In Figure 8, one can see that an optimal convergence order is obtained. The estimated convergence orders of the HDG method with an affine mapping, a quadratic mapping and a cubic mapping are summarized in Table 6. The contour lines of  $E_z$  and  $\mathbf{H}_x$  are displayed in Figure 9. From Figure 9, we find that for the affine mapping, the largest errors are located on the elements near the curved boundary, and then spread all over the computational domain. For high order mappings, we do not have this observation. The use of an high order isoparametric mapping is the key to the success of high order HDG schemes when the computational domain has curved boundaries. In the case of affine mapping, the geometric error dominates, which makes the asymptotic convergence order bounded by 2.

A comparison between the performance of the HDG method and the upwind flux DG method is given in Table 7. We use the same notations as in Table 2. In addition, for “ $T_{\text{construction}}$ ”, “-A” denotes the CPU time spent for the construction of the linear system with affine mapping, while “-C” denotes that with

Table 5: Triangular meshes used for the scattering of a plane wave by a metallic cylinder.

Mesh	Mesh size $h$	$N_t$	$N_{sf}$	$N_{cf}$
M1	0.660	314	439	64
M2	0.372	1278	1853	128
M3	0.191	5040	7432	256
M4	0.096	20234	30095	512

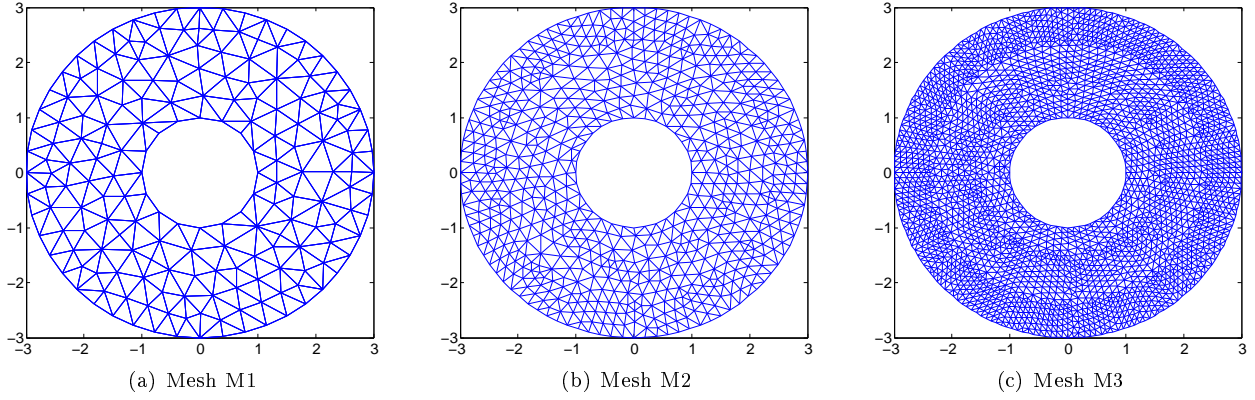


Figure 6: Trainagular meshes for the scattering of a plane wave by a metallic cylinder.

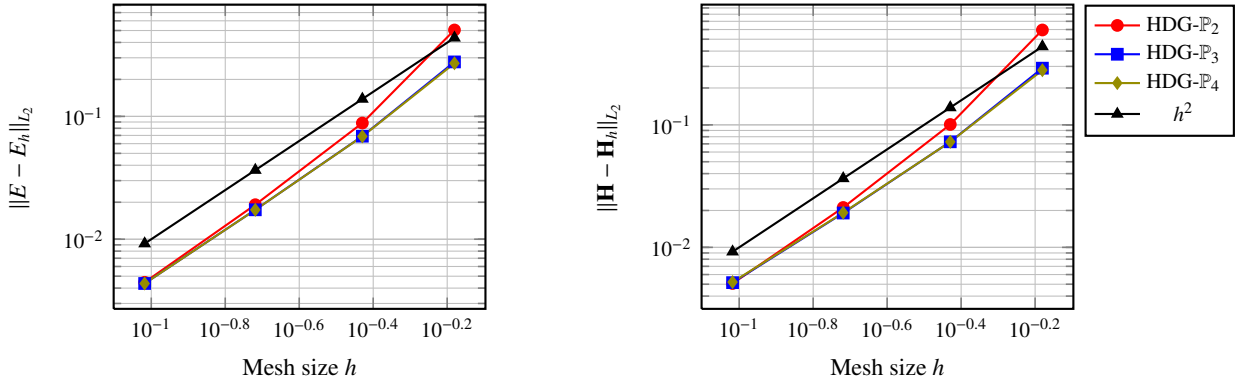


Figure 7: Convergence history of the HDG method with affine mapping.

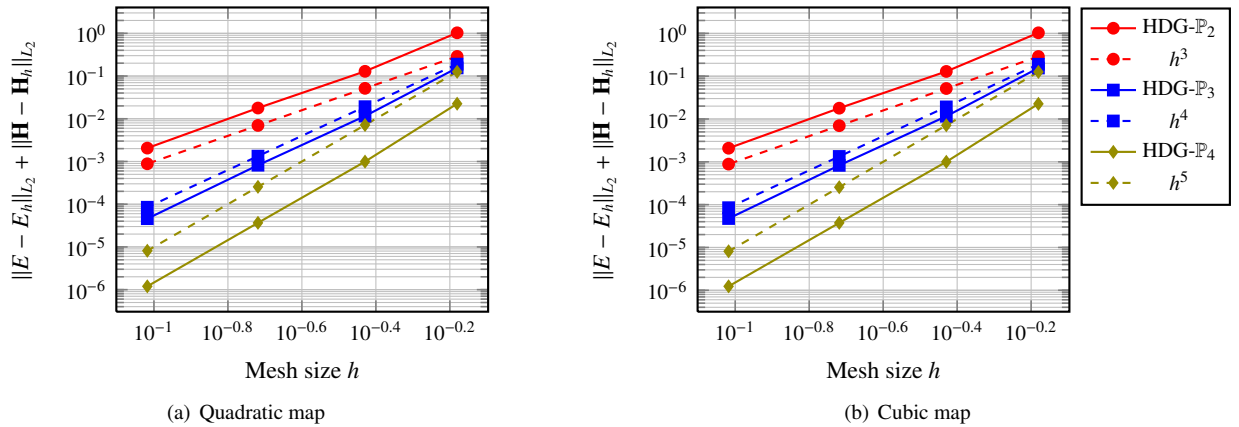


Figure 8: Convergence history of the HDG method with high order mappings. The convergence properties are nearly the same with both quadratic and cubic mappings for  $\mathbb{P}_2$ ,  $\mathbb{P}_3$  and  $\mathbb{P}_4$  schemes. This is probably because in this test case both quadratic mapping and cubic mapping can well represent the boundary arcs.

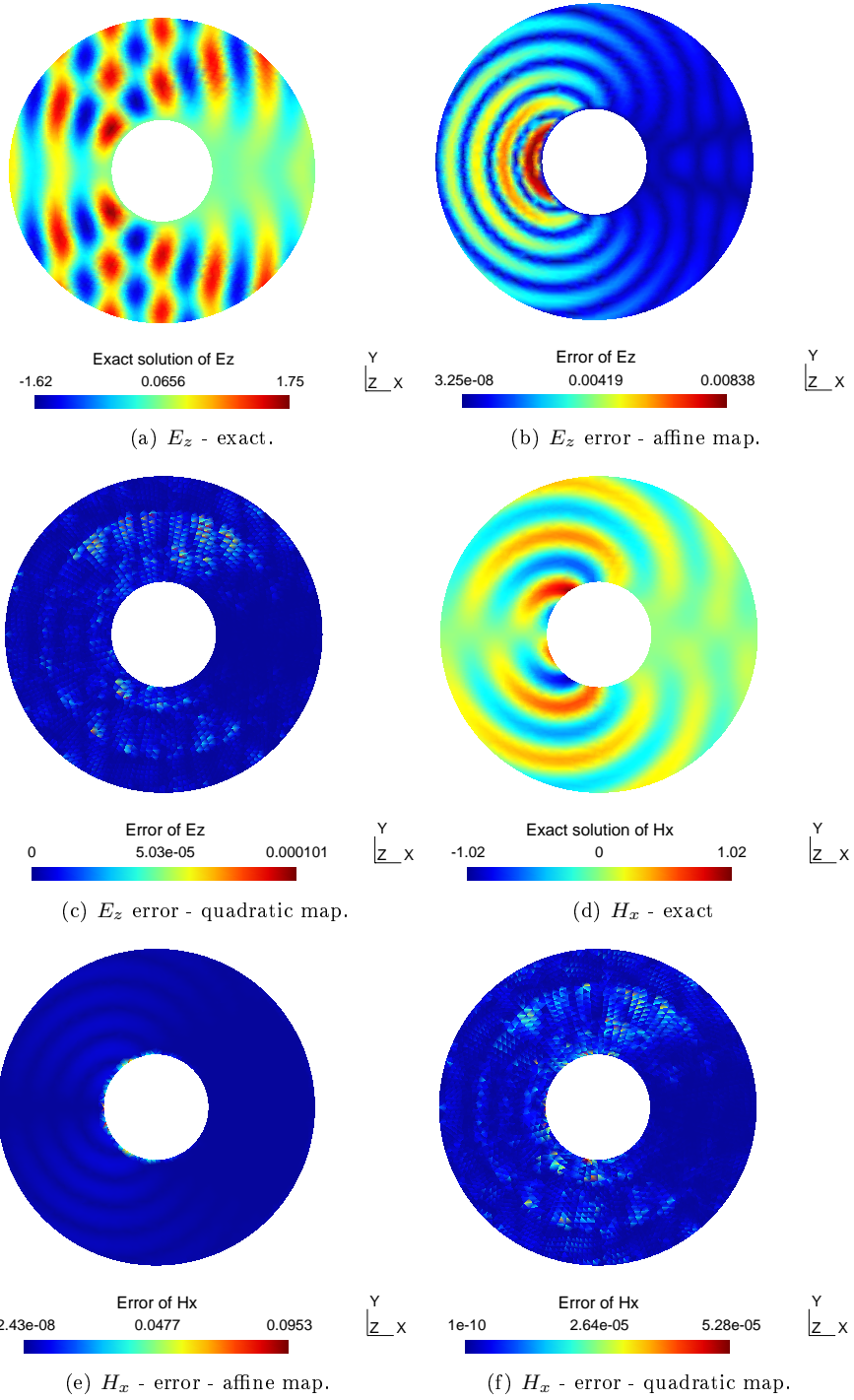


Figure 9: Contour lines of the fields and errors for the scattering of a plane wave by a metallic cylinder. Simulations are performed using the HDG- $\mathbb{P}_4$  method with affine map and quadratic map on mesh M3.

Table 6: Numerical convergence order of the HDG method for the scattering of a plane wave by a metallic cylinder.

	Affine map		Quadratic map		Cubic map	
	$E$	$\mathbf{H}$	$E$	$\mathbf{H}$	$E$	$\mathbf{H}$
P2	2.4	2.4	3.2	3.2	3.2	3.2
P3	2.1	2.1	4.2	4.2	4.2	4.1
P4	2.1	2.1	5.1	5.1	5.1	5.0

cubic mapping. The memory and CPU time cost for the solution of the linear systems are the same with different isoparametric mappings. Compared to the total CPU time spent for the construction of the globally coupled linear system, the extra CPU time spent on high order mappings is very small. We can make similar observations from Table 7 as from Table 2. Moreover, on the finest mesh, the linear systems obtained from UF- $\mathbb{P}_3$  and UF- $\mathbb{P}_4$  cannot be solved by MUMPS due to the large number of globally coupled DOFs, so we use “-” to denote the unknown memory and CPU time costs.

Table 7: Comparisons between HDG and upwind flux DG methods on memory and CPU time.

Mesh	Memory (MB)		$T_{\text{construction}}$ (s)				$T_{\text{solution}}$ (s)	
	HDG	UF	HDG-A	HDG-C	UF-A	UF-C	HDG	UF
$\mathbb{P}_1$								
M1	2	9	0.00	0.00	0.00	0.00	0.01	0.04
M2	7	42	0.01	0.01	0.00	0.01	0.03	0.25
M3	29	197	0.04	0.03	0.01	0.01	0.15	1.5
M4	134	942	0.16	0.16	0.04	0.04	0.84	10.4
$\mathbb{P}_2$								
M1	4	22	0.02	0.01	0.00	0.00	0.01	0.15
M2	14	109	0.04	0.04	0.01	0.02	0.06	0.91
M3	61	514	0.16	0.16	0.03	0.03	0.33	5.41
M4	285	2408	0.61	0.62	0.13	0.13	2.04	37.3
$\mathbb{P}_3$								
M1	5	43	0.03	0.03	0.01	0.01	0.01	0.30
M2	23	211	0.12	0.13	0.02	0.03	0.10	1.85
M3	106	1003	0.47	0.49	0.07	0.08	0.62	12.5
M4	497	-	1.93	1.95	0.30	0.32	4.01	-
$\mathbb{P}_4$								
M1	7	76	0.08	0.09	0.01	0.02	0.02	0.56
M2	35	364	0.32	0.34	0.05	0.05	0.18	3.49
M3	162	1679	1.28	1.33	0.15	0.18	1.05	23.1
M4	771	-	5.13	5.20	0.62	0.68	7.39	-

### 6.3 Scattering of a plane wave by a dielectric cylinder

We finally consider the problem of the scattering of a plane wave by a dielectric cylinder. The incident frequency is 300 MHz. The relative permittivity of the dielectric cylinder is 2.25. The radius of the dielectric cylinder is 1. The artificial absorbing boundary is set to be a concentric circle with radius 3. A quadratic mapping is employed to deal with the curved boundaries e.g. the boundary of the dielectric cylinder and that of the artificial boundary. We use four independently refined meshes whose characteristics are summarized in Table 8, where  $N_v$ ,  $N_t$  and  $N_f$  respectively denote the number of vertices, elements and faces (straight

and curved). The convergence results are presented in Table 9. We find that the optimal convergence rate is obtained on refined meshes for all the HDG- $\mathbb{P}_i$ ,  $i = 1, 2, 3, 4$  methods. But if an affine mapping is employed on the entire mesh, the convergence rate is confined to 2. The last three meshes are shown in Figure 10.

Table 8: Triangular meshes used for the scattering of a plane wave by a dielectric cylinder.

Mesh	Mesh size $h$	$N_v$	$N_t$	$N_f$
M1	1.167	59	92	150
M2	0.684	201	352	552
M3	0.384	795	1432	2196
M4	0.185	2945	5696	8640

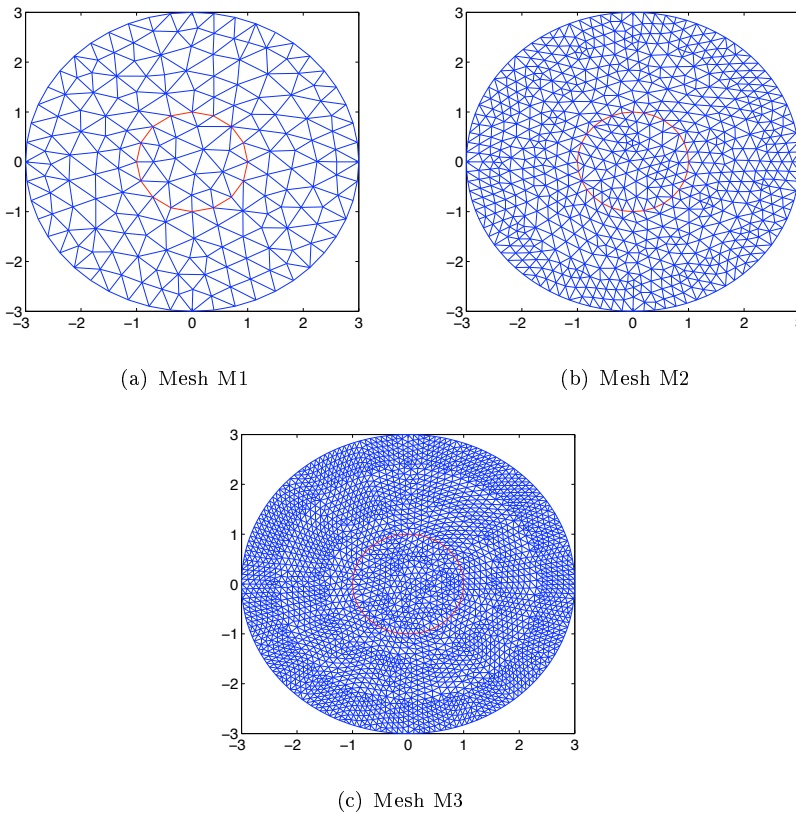


Figure 10: Triangular meshes for the scattering of a plane wave by a dielectric cylinder.

## 7 Concluding remarks and future works

In this paper, we have studied a hybridizable discontinuous Galerkin method for the numerical solution of the time-harmonic Maxwell equations in 2d. The HDG method is developed directly for the first order (mixed) form of Maxwell's equations, from which we can obtain the approximate solutions to both electric and magnetic fields. In this HDG method, we are required to solve local problems on every element to get the solutions for the fields and a global system to obtain the solution for the hybrid variable. The proposed method has been shown to be locally conservative. The well-posedness of the local problems for the HDG- $\mathbb{P}_1$

Table 9: Numerical convergence order of the HDG method for the scattering of a plane wave by a dielectric cylinder.

Mesh	$\mathbb{P}_1$				$\mathbb{P}_2$			
	$\ E - E_h\ _{L^2}$		$\ \mathbf{H} - \mathbf{H}_h\ _{L^2}$		$\ E - E_h\ _{L^2}$		$\ \mathbf{H} - \mathbf{H}_h\ _{L^2}$	
	Error	Order	Error	Order	Error	Order	Error	Order
M1	3.96e+00	-	4.30e+00	-	3.07e+00	-	3.45e+00	-
M2	2.52e+00	0.8	2.78e+00	0.8	1.34e+00	1.5	1.56e+00	1.5
M3	1.46e+00	0.9	1.64e+00	0.9	1.27e-01	4.1	1.63e-01	3.9
M4	2.97e-01	2.2	3.40e-01	2.2	1.11e-02	3.3	1.64e-02	3.2
Mesh	$\mathbb{P}_3$				$\mathbb{P}_4$			
	$\ E - E_h\ _{L^2}$		$\ \mathbf{H} - \mathbf{H}_h\ _{L^2}$		$\ E - E_h\ _{L^2}$		$\ \mathbf{H} - \mathbf{H}_h\ _{L^2}$	
	Error	Order	Error	Order	Error	Order	Error	Order
M1	1.98e+00	-	2.38e+00	-	6.49e-01	-	7.37e-01	-
M2	2.23e-01	4.1	2.87e-01	3.9	2.98e-02	5.8	4.45e-02	5.3
M3	1.09e-02	5.2	1.72e-02	4.9	1.18e-03	5.6	2.15e-03	5.3
M4	5.79e-04	4.0	9.52e-04	4.0	3.10e-05	5.0	5.23e-05	5.1

and HDG- $\mathbb{P}_2$  methods is assured. The assembly of the reduced system is similar to a classical finite element assembly and the reduced system has a wave equation-like nature which results in an indefinite global linear system. The numerical results show that the approximate solutions for both  $E$  and  $\mathbf{H}$  fields have optimal convergence order. Compared to a standard upwind flux-based DG method, the HDG method can reduce the memory cost and the computing CPU time, because of the reduction of the number of globally coupled degrees of freedom.

In addition, an isoparametric mapping technique combined with the proposed high order HDG formulation has been discussed for handling curvilinear geometries. Numerical experiments have shown that high order isoparametric mappings play an essential role for the high order accuracy of the HDG methods. With an affine geometric approximation, we can only have second order accuracy for high order HDG methods. With quadratic or cubic mappings, the optimal convergence order of high order HDG method can be retained.

The encouraging results obtained here in 2d naturally motivate the development of a high order HDG method for the system of 3d time-harmonic Maxwell equations. Indeed, this is the ultimate objective of our investment in hybridizable DG methods for the numerical solution of time-harmonic electromagnetic wave propagation involving irregularly shaped objects and complex media. In the 3d case, several issues have to be considered simultaneously: the design of a locally well-posed HDG formulation of the system of partial differential equations at hand; the choice of an appropriate high order interpolation method in view of  $hp$ -adaptivity; the numerical treatment of curved boundaries; the design of an appropriate, ideally parallel, solution strategy for the resulting global linear system for the hybrid variable; and, the definition of a parallelization strategy for taking full benefit of the local character of the HDG method. Concerning the last point, a very appealing approach is to combine a SIMD (Single Instruction Multiple Data) fine grain parallelism with a MIMD (Multiple Instruction Multiple Data) coarse grain parallel model, in particular for exploiting modern heterogeneous multicore parallel systems.

The development of such a high order HDG method for the system of 3d time-harmonic Maxwell equations is as a matter of fact underway. For large-scale problems, the solution strategy that we will adopt is based on domain decomposition principles building upon previous works on Schwarz algorithms (Dolean *et al.*, 2008). To conclude, and to give a first illustration of the capabilities of the method in 3d, we provide here preliminary results, considering again the model problem of the propagation of a plane wave in the vacuum. The computational domain is chosen to be the unit cube  $\Omega = ]-0.5; 0.5[^3$  and the Silver Müller absorbing boundary condition is imposed on the whole  $\partial\Omega$ . For this test problem, we employ a Matlab implementation of the HDG- $\mathbb{P}_1$  and HDG- $\mathbb{P}_2$  methods with nodal Lagrange basis expansions on tetrahedral elements. A sequence of regular tetrahedral meshes are employed, which divide the unit cube into  $(N_x - 1) \times (N_y - 1) \times (N_z - 1)$  little cubes, where  $N_x$ ,  $N_y$  and  $N_z$  are the number of grid points on the

edges of the unit cube, and then each little cube is divided into 6 tetrahedrons. Table 10 summarizes the error and convergence behaviors of both the HDG- $\mathbb{P}_1$  and HDG- $\mathbb{P}_2$  methods. In Table 10, «Mesh size» denotes the edge length of the tetrahedrons on the edge of the unit cube (we set  $N_x = N_y = N_z$  in the construction of the tetrahedral meshes) and  $N_{dof}$  stand for the total number of degrees of freedom. We observe that the convergence orders of the approximate solutions for both  $\mathbf{E}$  and  $\mathbf{H}$  seems to be optimal as it was the case in 2d. These results with more details on the formulation can be found in (Li *et al.*, 2011).

Table 10: Propagation of a plane wave in vacuum: numerical convergence of the HDG- $\mathbb{P}_1$  and HDG- $\mathbb{P}_2$  methods.

Mesh size $h$	$N_{dof}$	$\ \mathbf{E} - \mathbf{E}_h\ _2$		$\ \mathbf{H} - \mathbf{H}_h\ _2$	
		Error	Order	Error	Order
HDG- $\mathbb{P}_1$					
1/2	720	2.27e-01	-	2.35e-01	-
1/4	5184	6.02e-02	1.9	6.68e-02	1.8
1/8	39168	1.54e-02	2.0	1.78e-02	1.9
HDG- $\mathbb{P}_2$					
1/2	1440	3.13e-02	-	3.36e-02	-
1/4	10368	4.00e-03	3.0	4.44e-03	2.9
1/8	78336	4.93e-04	3.0	5.53e-04	3.0

## References

- Amestoy, P., Duff, I. and L'Excellent J.Y. (2000), «Multifrontal parallel distributed symmetric and unsymmetric solvers », *Comput. Meth. Appl. Mech. Eng.*, Vol. 184, 501-520.
- Arnold, D.N., Brezzi, B., Cockburn, B. and Marini, L.D. (2002), «Unified analysis of discontinuous Galerkin methods for elliptic problems », *SIAM J. Numer. Anal.*, Vol. 39, No. 5, 1749-1779.
- Bassi, F. and Rebay, S. (1997), «High order accurate discontinuous finite element solution of the 2d Euler equations », *J. Comput. Phys.*, Vol. 138, No. 2, 251-285.
- Cockburn, B. and Shu, C.-W. (1989), «TVB Runge-Kutta local projection discontinuous Galerkin finite element method for conservation laws II: general framework », *Math. Comp.*, Vol. 52, 411-435.
- Cockburn, B. and Shu, C.-W. (1998), «The local discontinuous Galerkin method for time-dependent convection-diffusion systems », *SIAM J. Numer. Anal.*, Vol. 35, No. 6, 2440-2463.
- Cockburn, B., Gopalakrishnan, J. and Lazarov R. (2009), «Unified hybridization of discontinuous Galerkin, mixed, and continuous Galerkin methods for second order elliptic problems », *SIAM J. Numer. Anal.*, Vol. 47, No. 2, 1319-1365.
- Cohen, G., Ferrieres, X. and Pernet, S. (2006), «A spatial high spatial order hexahedral discontinuous Galerkin method to solve Maxwell's equations in time-domain », *J. Comput. Phys.*, Vol. 217, No. 2, 340-363.
- Cools, R. (2003), «An encyclopaedia of cubature formulas », *J. Complexity*, Vol. 19, 445-453,
- Dolean, V., Fol, H., Lanteri, S. and Perrussel, P. (2008), «Solution of the time-harmonic Maxwell equations using discontinuous Galerkin methods », *J. Comput. Appl. Math.*, Vol. 218, 435-445.
- Dolean, V., Lanteri, S. and Perrussel, P. (2008), «A domain decomposition method for solving the three-dimensional time-harmonic Maxwell equations discretized by discontinuous Galerkin methods », *J. Comput. Phys.*, Vol. 227, No. 3, 2044-2072.

- Fahs, H. (2010), «Discontinuous Galerkin method for time-domain electromagnetics on curvilinear domains », *Appl. Math. Sci.*, Vol. 4, No. 19, 943-958.
- Feng, X. and Wu, H. (2009), «Discontinuous Galerkin method for Helmholtz equation with large wave numbers », *SIAM J. Numer. Anal.*, Vol. 47, No. 4, 2872-2896.
- Feng, X. and Xing, Y. (2012), «Absolutely stable local discontinuous Galerkin methods for the Helmholtz equation with large wave number », *Math. Comp.*, to appear.
- Fezoui, L., Lanteri, S., Lohrengel, S. and Piperno, S. (2005), «Convergence and stability of a discontinuous Galerkin time-domain method for the 3D heterogeneous Maxwell equations on unstructured meshes», *RAIRO: M2AN*, Vol. 39, No. 6, 1149-1176.
- Griesmaier, R. and Monk, P. (2011), «Error analysis for a hybridizable discontinuous Galerkin method for the Helmholtz equation », *J. Sci. Comput.*, Vol. 49, No. 3, 291-310.
- Hesthaven, J.S. and Warburton, T. (2002), «Nodal high-order methods on unstructured grids. I. Time-domain solution of Maxwell's equations », *J. Comput. Phys.*, Vol. 181, No. 1, 186-221.
- Hesthaven, J.S. and Warburton, T. (2008), «Nodal discontinuous Galerkin methods - algorithms, analysis, and applications », Springer, New York.
- Houston, P., Perugia, I. A. and Schotzau, A. (2004), «Mixed discontinuous Galerkin approximation of the Maxwell's equations », *SIAM J. Numer. Anal.*, Vol. 42, No. 1, 434-459.
- Houston, P., Perugia, I., Schneebeli, A. and Schotzau, A. (2005), «Interior penalty method for the indefinite time-harmonic Maxwell's equations », *Numer. Math.*, Vol. 100, 485-518.
- Kirby, R.M., Sherwin, S.J. and Cockburn, B. (2012), «To CG or to HDG: a comparative study », *J. Sci. Comput.*, Vol. 51, No. 1, 183-212.
- Krivodonova, L. and Berger, M. (2006), «High-order accurate implementation of solid wall boundary conditions in curved geometries », *J. Comput. Phys.*, Vol. 211, No. 2, 492-512.
- Li, L., Lanteri, S., and Perrussel, P. (2011), «A hybridizable discontinuous Galerkin method for solving 3D time-harmonic Maxwell's equations », to appear in the Proceedings of Enumath 2011, Leicester (UK).
- Lanteri, S., Li L. and Perrussel, P. (2011), «A hybridizable discontinuous Galerkin method for time-harmonic Maxwell's equations », INRIA Reserach Report RR-7649.
- Luo, X.J., Shephard, M.S. and Remacle, J.F. (2001), «The influence of geometric approximation on the accuracy of high order methods », Rensselaer SCOREC report, No. 1, pp. 1-10.
- Nedelec, J.C. (1986), «A new family of mixed finite elements in  $\mathbb{R}^3$  », *Numer. Math.*, Vol. 50, No. 1, 57-81.
- Nguyen, N.C., Peraire J. and Cockburn B. (2009a), «An implicit high-order hybridizable discontinuous Galerkin method for linear convection-diffusion equations », *J. Comput. Phys.*, Vol. 228, No. 9, 3232-3254.
- Nguyen, N.C., Peraire J. and Cockburn B. (2009b), «An implicit high-order hybridizable discontinuous Galerkin method for nonlinear convection-diffusion equations », *J. Comput. Phys.*, Vol. 228, No. 23, 8841-8855.
- Nguyen, N.C., Peraire J. and Cockburn B. (2011), «Hybridizable discontinuous Galerkin methods for the time-harmonic Maxwell's equations », *J. Comput. Phys.*, Vol. 230, No. 19, 7151-7175.
- Solin, P., Segeth, K. and Dolezel, I. (2004), «Higher-order finite element methods », Studies in Advanced Mathematics, Chapman & Hall/CRC.

Zláamal, M. (1973), «Curved elements in finite element method », *SIAM J. Numer. Anal.*, Vol. 10, No. 1, 229-240.